Draft version June 16, 2023

Typeset using LaTeX **twocolumn** style in AASTeX631

Gasing Pangkah I: Asteroseismic Identification and Characterisation of a Rapidly-Rotating Engulfment Candidate

J. M. Joel Ong (王加冕) ,[1,*] Marc Teng Yen Hon,[1,*] Melinda Soares-Furtado,[2,3,*] Alexander P. Stephan,[4,5] Jennifer van Saders,[1] Jamie Tayar,[6] Benjamin Shappee,[1] Daniel R. Hey,[1] Lyra Cao,[4] Mutlu Yildiz,[7] Zeynep Çelik Orhan,[7] Sibel Örtel,[7] Benjamin Montet,[8,9] Christopher Kochanek,[4] Subo Dong (东苏勃),[10] Jose Prieto,[11] Thomas W.-S. Holoien,[12] Joss Bland-Hawthorn,[13,14] Sven Buder,[15,14] Gayandhi M. De Silva,[16] Ken C. Freeman,[15,14] Michael R. Hayden,[13,14] Janez Kos,[17] Sarah L. Martell,[8,14] Geraint F. Lewis,[13] Karin Lind,[18] Sanjib Sharma,[19] Dennis Stello,[8,13,14,20] Daniel B. Zucker,[21,22,14] and Tomaž Zwitter[17]

[1]*Institute for Astronomy, University of Hawai'i, 2680 Woodlawn Drive, Honolulu, HI 96822, USA*
[2]*Department of Astronomy, University of Wisconsin-Madison, 475 N. Charter St., Madison, WI 53703, USA*
[3]*MIT Kavli Institute for Astrophysics and Space Research, 77 Massachusetts Ave., Cambridge, MA 02139, USA*
[4]*Department of Astronomy, The Ohio State University, Columbus, OH 43210, USA*
[5]*Center for Cosmology and Astroparticle Physics, The Ohio State University, Columbus, OH 43210, USA*
[6]*Department of Astronomy, University of Florida, Bryant Space Science Center, Stadium Road, Gainesville, FL 32611, USA*
[7]*Department of Astronomy and Space Sciences, Science Faculty, Ege University, 35100, Bornova, İzmir, Turkey*
[8]*School of Physics, University of New South Wales, Sydney, NSW 2052, Australia*
[9]*UNSW Data Science Hub, University of New South Wales, Sydney, NSW 2052, Australia*
[10]*Kavli Institute for Astronomy and Astrophysics, Peking University, Beijing 100871, PRC*
[11]*Instituto de Estudios Astrofísicos, Universidad Diego Portales, Av. Ejército Libertador 441, Santiago, Chile*
[12]*Carnegie Observatories, 813 Santa Barbara Street, Pasadena, CA 91101 USA*
[13]*Sydney Institute for Astronomy, School of Physics, A28, The University of Sydney, NSW 2006, Australia*
[14]*ARC Centre of Excellence for All Sky Astrophysics in 3 Dimensions (ASTRO 3D), Australia*
[15]*Research School of Astronomy and Astrophysics, Australian National University, Canberra, ACT 2611, Australia*
[16]*Australian Astronomical Optics, Macquarie University, 105 Delhi Rd, North Ryde, NSW 2113, Australia*
[17]*Faculty of Mathematics and Physics, University of Ljubljana, Jadranska 19, 1000 Ljubljana, Slovenia*
[18]*Department of Astronomy, Stockholm University, AlbaNova University Centre, SE-106 91 Stockholm, Sweden*
[19]*Space Telescope Science Institute, 3700 San Martin Drive, Baltimore, MD, 21218, USA*
[20]*Stellar Astrophysics Centre, Aarhus University, Ny Munkegade 120, DK-8000 Aarhus C, Denmark*
[21]*Department of Physics and Astronomy, Macquarie University, Sydney, NSW 2109, Australia*
[22]*Macquarie University Research Centre for Astronomy, Astrophysics and Astrophotonics, Sydney, NSW 2109, Australia*

(Dated: June 16, 2023)

ABSTRACT

We report the discovery and characterisation of TIC 350842552 ("Zvrk"), an apparently isolated, rapidly-rotating ($P_{\rm rot} \sim 99$ d) red giant observed by TESS in its Southern Continuous Viewing Zone. The star's fast surface rotation is independently verified by the use of p-mode asteroseismology, strong periodicity in TESS and ASAS-SN photometry, and measurements of spectroscopic rotational broadening. A two-component fit to APOGEE spectra indicates a coverage fraction of its surface features consistent with the amplitude of the photometric rotational signal. Variations in the amplitude of its photometric modulations over time suggest the evolution of its surface morphology, and therefore enhanced magnetic activity. We further develop and deploy new asteroseismic techniques to characterise radial differential rotation, and find weak evidence for rotational shear within Zvrk's convective envelope. This feature, in combination with such a high surface rotation rate, is incompatible with even the most physically permissive models of angular-momentum transport in single-star evolution. Spectroscopic abundance estimates also indicate a near-meteoritic lithium abundance, among other chemical anomalies. Taken together, all of these suggest an ingestion scenario for the formation of this rotational configuration, various models for which we examine in detail.

Keywords: Asteroseismology (73), Red giant stars (1372), Stellar oscillations (1617)

Corresponding author: Joel Ong
joelong@hawaii.edu

[*] NASA Hubble Fellow

1. INTRODUCTION

Single-star evolution predicts the development of radial differential rotation during a star's first ascent up the red giant branch, in the sense of there being a faster-rotating radiative core than convective envelope. While seismic rotational measurements with evolved stars indicate that subgiant convective envelopes rotate faster than strict angular momentum conservation would suggest (e.g. Mosser et al. 2012; Triana et al. 2017; Deheuvels et al. 2020), envelope rotation rates nonetheless are predicted to further decrease dramatically as red giants expand, making them challenging to measure for more evolved red giants at higher luminosity. Indeed, many existing techniques for seismic rotation measurements in these evolved stars assume a priori that the rotation of the stellar envelope may be ignored (e.g. Gehan et al. 2018; Mosser et al. 2018). In the regime of (relatively) strong coupling between the interior g-mode cavity to the exterior p-mode cavity, this simplifying assumption has enabled the measurement of core rotation rates in red giants of intermediate luminosity in the *Kepler* sample en masse, at the expense of sacrificing information about the surface rotation of these stars. Since the surfaces of red giants are not expected to rotate in any significant fashion, such a loss of sensitivity is ordinarily considered acceptable.

Contrary to this expectation, a small fraction of the *Kepler* red giant sample does exhibit nontrivial photometric variability, attributable to surface features rotating into and out of view (e.g. Tayar et al. 2015; Ceillier et al. 2017). Rotation rates as high as these are not generally compatible with standard descriptions of angular momentum transport constructed to describe less evolved stars (Aerts et al. 2019; Fuller et al. 2019), and indicate that these rapidly-rotating red giants (RRRGs) may have passed through evolutionary scenarios quite unlike the standard picture of single-star evolution (e.g. Massarotti et al. 2008; Carlberg et al. 2011). In particular, such stars are thought possibly to have been spun up as a result of binary interactions (e.g. Tayar et al. 2015; Casey et al. 2019) or engulfment events (Lau et al. 2022; O'Connor et al. 2023). The latter would be associated with overabundance in light elements such as lithium in the envelopes of first ascent red giants (e.g. Aguilera-Gómez et al. 2016a,b; Soares-Furtado et al. 2021), and may illuminate the evolution of late-stage planetary systems (e.g. De et al. 2023).

Similarly to main-sequence stars, we expect that asteroseismic constraints on surface rotation in evolved stars will be provided by their exterior p-mode cavity, rather than through the interior g-modes that are typically measured. While coupling between the two mode cavities prevents direct measurement of these pure p-mode frequencies, the strength of this coupling in first-ascent red giants decreases dramatically with evolution (e.g. Farnir et al. 2021; Jiang et al. 2022; Ong & Gehan 2023). The frequencies of p-dominated mixed modes therefore become observationally indistinguishable from those of the pure p-modes underlying them in higher-luminosity RRRGs, which are in any case mostly convective by spatial extent. Although traditional computational methods for mixed-mode asteroseismology — and in particular those which relate mode frequencies to interior structure — have been very expensive to apply to these most highly luminous red giants (Christensen-Dalsgaard et al. 2020), recent theoretical developments now permit the numerical analysis of red-giant p-modes to be performed in a likewise decoupled fashion from the interior g-mode cavity, thereby circumventing these computational difficulties (Ball et al. 2018; Ong & Basu 2020).

RRRGs are frequently observed to have suppressed oscillations, making asteroseismic characterisation of them challenging. This suppression is often also attributed to tidal synchronisation with a close companion (Gaulme et al. 2020). Conversely, the overwhelming majority of evolved RRRGs which do exhibit pulsations do not have detectable orbital companions (ibid.), rendering their rotation all the more difficult to explain. Owing to these unfavourable observing conditions, and the above-described difficulties in observational and numerical methodology, these pulsating RRRGs have so far not been subjected to detailed asteroseismic constraints on their internal structure and rotation.

In this context, we report the contemporaneous detection and characterisation of both rotational and asteroseismic signals in TIC 350842552 (which we will refer to informally as "Zvrk"[1] in the remainder of this work, for brevity), a highly evolved and most likely standalone RRRG. Asteroseismology (from the NASA TESS mission), direct photometry (both from TESS, and separately with the ground-based ASAS-SN network), and spectroscopy (various ground-based spectrographs) all independently confirm its rapid rotation, with a 99-day period as measured in photometry. Zvrk's spectroscopic chemical abundances also exhibit peculiarities that are difficult to explain by way of single-star evolutionary modelling. In addition, Zvrk is far more evolved than almost the entire *Kepler* sample of RRRGs (Ceillier et al. 2017), such that all of its observed modes may be well approximated as being pure p-modes. This permits us to bring to bear new analytic developments in the interpretation of rotational signatures derived from p-mode oscillations in this red giant. Rather than characterising a two-zone core-vs-envelope rotational contrast as is typically examined in less evolved red giants, we find instead weak evidence for radial differential rotation situated entirely within Zvrk's convective envelope. Zvrk's high rotation rate, possible rotational shear, and anomalous chemical abundances are highly suggestive of an ingestion scenario for its formation, on which we place preliminary constraints. We conclude with some discussion about the astrophysical significance of this finding, methodological implications of the techniques that were developed for this work, and suggestions for future work.

2. OBSERVATIONAL CHARACTERISATION

[1] Serbo-Croat: "spinning top"

Zvrk was initially flagged for asteroseismic analysis as part of an ongoing large-scale search for unusual oscillation signatures corresponding to chemical peculiarities, in particular high lithium abundance. For this purpose, an overlapping sample of stars with both preliminary GALAH DR4 lithium abundance estimates, and TESS coverage in the Southern continuous viewing zone (CVZ), was constructed (Montet et al., in prep). Targets in this list were subjected to preliminary asteroseismic analysis, to constrain the global p-mode asteroseismic parameters $\Delta\nu$ and $\nu_{\rm max}$. This was done using the 2D autocorrelation function technique (2DACF: Viani et al. 2019), applied to the SPOC light curves from the first two Southern CVZ campaigns in TESS Cycles 1 and 3. For Zvrk in particular, this procedure yielded $\Delta\nu = (1.23 \pm 0.01)\ \mu$Hz; $\nu_{\rm max} = (7.5 \pm 0.3)\ \mu$Hz.

Among this sample, Zvrk stood out because of an unusually large surface lithium abundance (A(Li) $\sim$ 3.2 dex; cf. Section 3.2). Also unusually for a red giant, it was observed by TESS at two-minute cadence: in Cycle 1 (Sectors 1-13), Cycle 3 (Sectors 27-39), and the ongoing Cycle 5. This allowed our analysis to be performed with respect to the publicly available presearch data conditioning simple aperture photometry (PDCSAP) lightcurves instead. Moreover, its power spectrum exhibits unusual features, whose structure departs significantly from that seen in similarly evolved red giants (e.g. Stello et al. 2014; Yu et al. 2020), and which defeated preliminary attempts at p-mode identification.

2.1. *Mode Frequencies and Rotational Splittings*

In order to proceed with further asteroseismic analysis, identifications for the integer indices n_p, ℓ, m must be assigned to such mode frequencies as are derived from the observed power spectrum. Morphologically, these double ridges on its frequency echelle diagram, Fig. 1, are evocative of those of other p-mode oscillators, as previously observed en masse with *Kepler* and TESS, and suggest identification as being modes of low, even degree ($\ell = 0, 2$), which are known in p-mode oscillators to form double ridges of this kind as a result of the p-mode asymptotic eigenvalue equation

$$\nu_{n_p\ell} \sim \Delta\nu\left(n_p + \frac{\ell}{2} + \epsilon_p\right) + \ell(\ell+1)\frac{\delta\nu_{02}}{6} + O(1/\nu), \qquad (1)$$

in the absence of rotation. Here $\Delta\nu$ and $\delta\nu_{02}$ are the large and small frequency separations from the standard phenomenological description of p-mode asteroseismology, and ϵ_p is a slowly-varying phase function. The remainder of the oscillation power would, under this putative identification, be attributed to oscillations of dipole modes, which are known in other red giants to be disrupted by mode mixing with an interior g-mode cavity, producing a complex forest of gravitoacoustic mixed modes. Visually, this morphology strongly resembles that seen in core-helium-burning stars, where the coupling between the interior g-mode and exterior p-mode cavities is known to be strong. Indeed, this is the mode identification also arrived at by the use of existing "data-driven" automated methods, trained on the *Kepler* sample of oscillating red giants (e.g. PBJam: Nielsen et al. 2021).

However, such an identification would be in significant tension with other known properties of stochastically-excited red giant oscillations. In particular:

- Red clump stars are known to yield much higher values of both $\Delta\nu$ and $\nu_{\rm max}$ than we have measured from Zvrk. Conversely, its $\Delta\nu$ and $\nu_{\rm max}$ are too high, and thus it is not evolved enough, to be an asymptotic giant branch star. The measured values of these quantities instead strongly favour classification of Zvrk as a first-ascent red giant.
- This mode identification would imply a radial p-mode phase offset of $\epsilon_p \sim 0.25$. However, the value of ϵ_p for radial modes in first-ascent red giants follows an extremely tight and robust relation with $\Delta\nu$, both in theoretical studies of stellar models (e.g. White et al. 2011; Ong & Basu 2019), as well as in existing large-scale characterisation of the *Kepler* sample (e.g. Mosser et al. 2011, Yu et al. 2020; cf. Figs. 10b and c of the latter). Thus, such a value of ϵ_p would be in significant tension with the value of 0.7 implied by the *Kepler* sample for red giants close to our nominal value of $\Delta\nu = 1.23\ \mu$Hz. We illustrate this in Fig. 1, where the position of the double-ridge feature in Zvrk's echelle power diagram can be seen to be offset from that shown for two other *Kepler* stars, both also first-ascent red giants.
- Both single-star stellar modelling (e.g. Deheuvels et al. 2022) and observational measurements (e.g. Mosser et al. 2014) of gravitoacoustic mixed modes in the *Kepler* sample also indicate that $\Delta\Pi_1$, the dipole-mode period spacing associated with the interior g-mode cavity, lies in a narrow band of allowed values with $\Delta\nu$ for first-ascent red giants. At this value of $\Delta\nu$, $\Delta\Pi_1$ would also be far too small, and the mixed-mode coupling strength be too weak, to cause significant departures in the frequencies of the observed dipole modes from those of simple p-modes. This can be seen to be the case for the two *Kepler* giants shown in Fig. 1, where the dipole modes can be seen to form a single ridge, indicating the observational unavailability of g-mode mixing. This being the case, we ought not to expect it to be available from Zvrk either.

We show instead in Fig. 2a our proposed alternative mode identification, which takes into account all of the above constraints from the *Kepler* field. By necessity, our radial modes are anchored by ϵ_p measurements from the *Kepler* field. To illustrate this, we show the average value of this quantity for all stars within 0.5 μHz of $\Delta\nu$ to Zvrk in the catalogue of Yu et al. (2020), and their standard deviation, using the white dashed line and red shaded interval, respectively.

In the presence of rotation, each mode at degree ℓ and radial order n_p splits into a $(2\ell+1)$-tuplet of peaks in the power spectrum, with the distribution of observed power between peaks

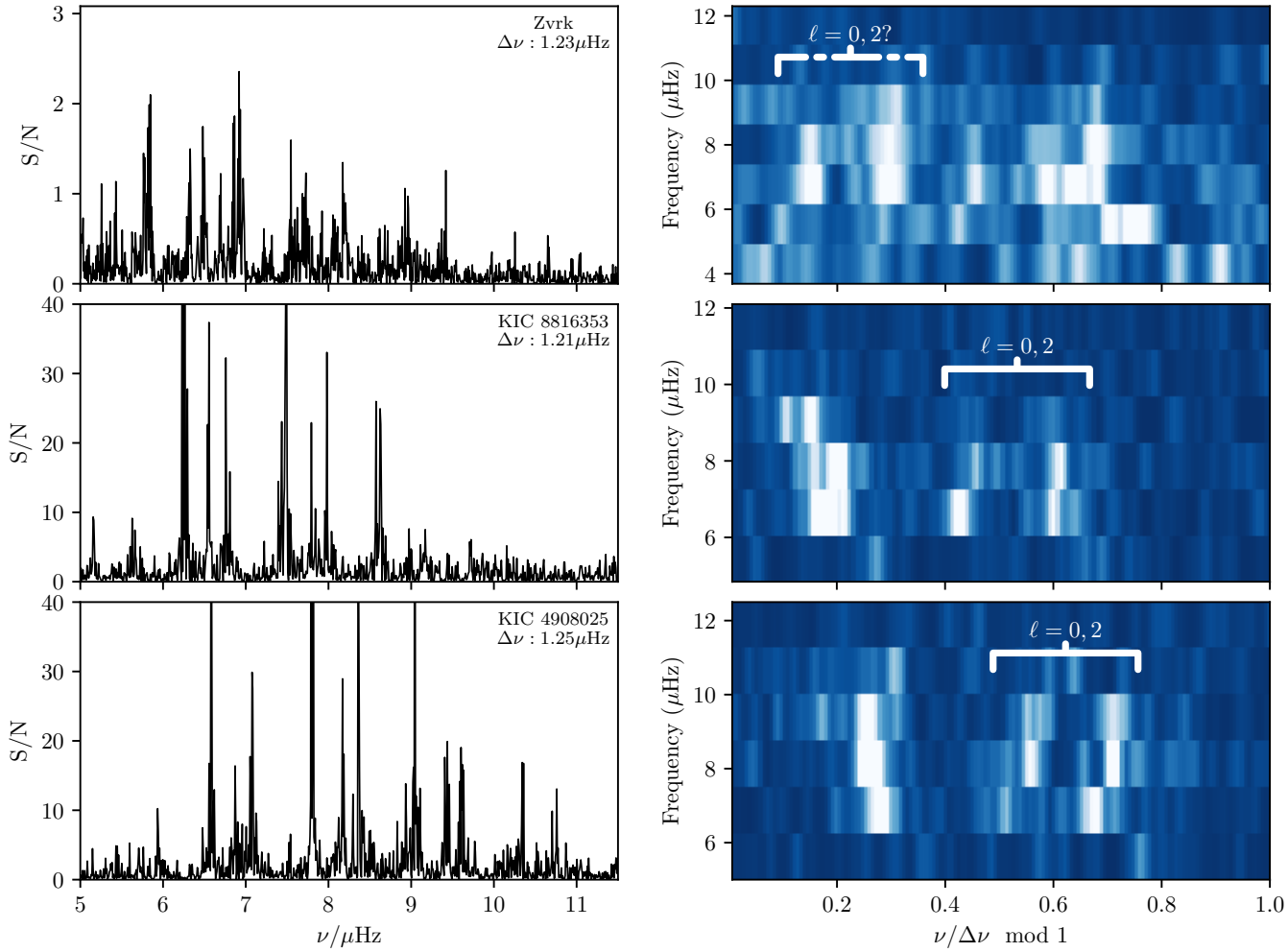

Figure 1. A comparison between Zvrk's oscillation power spectra with those from Kepler red giants KIC 8816353 and KIC 4908025. The oscillation spectra of the Kepler red giants show the expected mode pattern for evolved red giants: three distinct ridges in the échelle diagram, with $l = 2, 0$ ridges centered at $\nu/\Delta\nu$ mod 1 ~ 0.6. In contrast, the power spectrum for Zvrk contains many additional peaks that does not conform to the expected mode pattern, with what was initially identified as the $l = 2, 0$ ridges located far from the typical value.

being determined by the inclination of the stellar rotational axis (Pesnell 1985; Gizon & Solanki 2003). Rather than being modes of even degree, we instead identify the double ridge as being rotationally-split doublets of dipole ($\ell = 1$) modes, viewed close to equator-on. In such an equator-on configuration, a mode of degree ℓ yields an $(\ell + 1)$-tuplet; our identification of the quadrupole modes must then be constrained by having to explain the remaining peaks using rotationally-split triplets. While our putative identification of the quadrupole modes is unfortunate from the perspective of fitting the rotational splittings (as the quadrupole-mode triplets straddle both the dipole and radial modes), this identification of the quadrupole modes is required for general consistency with the values of r_{02} typically returned from stellar models with comparable $\Delta\nu$ (e.g. White et al. 2011). Moreover, in keeping with the star's evolved state, all of these modes are proposed to be essentially decoupled from the interior g-mode cavity.

Since g-mode mixing is not an observational concern, we may directly repurpose existing techniques for the derivation of p-mode frequencies from power spectra — peakbagging — to this star. For this purpose, we fit an ansatz model in the form

$$f(\nu) = \sum_i \sum_{m=-\ell_i}^{\ell_i} \frac{H_i r(m, \ell_i, i_\star)}{1 + (\nu_i + m\delta\nu_i - \nu)^2/\Gamma_i^2} + \mathrm{BG}(\nu) \qquad (2)$$

directly to the power spectrum. The asteroseismic component of this power spectral model can be seen to be a sum of Lorentzians parameterised by the nonrotating frequencies ν_i, the mode heights H_i, the inverse mode lifetimes Γ_i, the rotational multiplet splittings $\delta\nu_i$, as well as the inclination $i_\star$ of the rotational axis (through the visibility ratios r of each multiplet component). In addition to this, we choose to describe our background model with a combination of a single Harvey profile and a white-noise term.

We seek to infer posterior distributions of all of these parameters in a Bayesian sense, which necessitates the imposition of

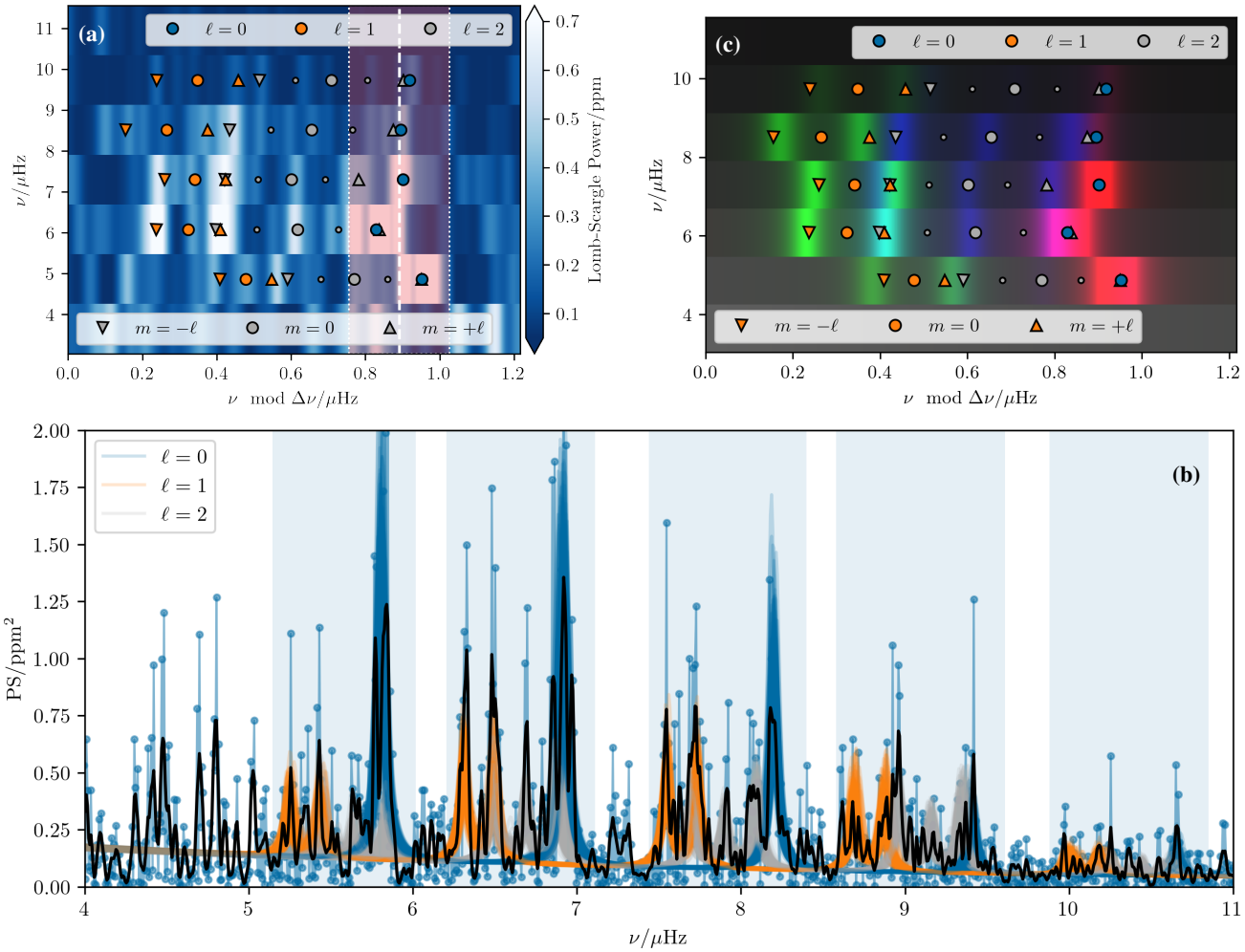

Figure 2. Asteroseismic characterisation of Zvrk. **(a)**: Échelle power diagram showing putative mode identification, manually constructed from naive peakfinding. The red shaded region indicates the allowable region for radial modes as implied by ϵ_p measurements from the *Kepler* field. **(b)**: Samples from the joint posterior distribution for all parameters describing our model of the power spectrum (semitransparent curves, Eq. (2); different colors show portions of the power spectrum attributed to modes of different degrees), overplotted against the raw power spectrum (filled circles joined with lines), and compared with a smoothed power spectrum (black line, corresponding to a Gaussian kernel of equal width to the resolution of the power spectrum, 0.007 μHz). **(c)**: RGB colour-channel échelle power diagram showing same samples from posterior distribution. The different colour channels show power attributed to modes of different degree: red for $\ell = 0$, green for $\ell = 1$, and blue for $\ell = 2$. Our original manual (not fitted) mode identification is overplotted for comparison. An animated version of this panel, to accommodate colourlind readers, is available in the online edition of this paper.

prior distributions. We place flat priors on each ν_i in windows 0.2 μHz wide, centered on each of the manually identified values shown in Fig. 2a; a flat prior on $\mu = \cos i_\star$ for isotropy; flat priors on the logarithms of the mode lifetimes, heights, and all parameters of our noise model; and flat priors on the widths of the rotational splittings. For our main analysis in this section we moreover pool the rotational splittings of the dipole and quadrupole modes separately, assigning either $\delta\nu_{\mathrm{rot},\ell=1}$ or $\delta\nu_{\mathrm{rot},\ell=2}$ to each nonradial mode depending on its degree ℓ_i. Additionally, we performed this exercise with and without pooling of the linewidths Γ_i. However, we found that, when linewidths were fitted on a per-mode basis, the posterior distributions of the linewidths for modes with low signal-to-noise ratios were very poorly constrained, and therefore permitted to take on unphysically large values at low amplitudes given our uninformative prior. In any case, the linewidths, which describe the damping rates of the modes, are not physically relevant for our following discussion, and their dependence on the mode frequency is weak at the low frequencies that we consider here. As such, we restrict our attention to results derived with a single linewidth Γ being fitted against all modes, to simplify our analysis.

With this parameterisation, these priors, and the standard likelihood function for describing values of the power spectrum P_j by the χ^2 distribution with 2 degrees of freedom (Anderson et al. 1990),

$$\mathcal{L}(\theta) \propto \exp\left[-\sum_j \left(\log f(\nu_j,\theta) + \frac{P_j}{f(\nu_j,\theta)}\right)\right], \quad (3)$$

in hand, we then use the nested-sampling Markov-Chain Monte-Carlo (MCMC) algorithm, as implemented in the `dynesty` Python package, to infer the posterior distribution implied by the TESS data. In Fig. 2b, we show 100 draws from the posterior distribution overplotted on the power spectrum, with contributions to Eq. (2) at different degree ℓ indicated with different colours of curves. The averages of these samples are shown with a colour-separated echelle power diagram in Fig. 2c, for easier graphical comparison with our mode identification by hand.

The fitted model power spectra shown in Fig. 2 can be seen to exhibit quite large rotational splitting, consistent with our initial hand-picked mode identification. More details about the results of this procedure can be found in the Appendix, where we show the joint posterior distributions for all pooled seismic quantities, as well as the parameters of our combined red- and white-noise background model (Fig. A1). There, we also report the medians and the widths of the 1σ credible regions of the posterior distributions for the fitted nonrotating ($m = 0$) mode frequencies in Table A1. From our radial mode frequencies alone, we re-fit $\Delta\nu$ to yield 1.21 ± 0.01 μHz.

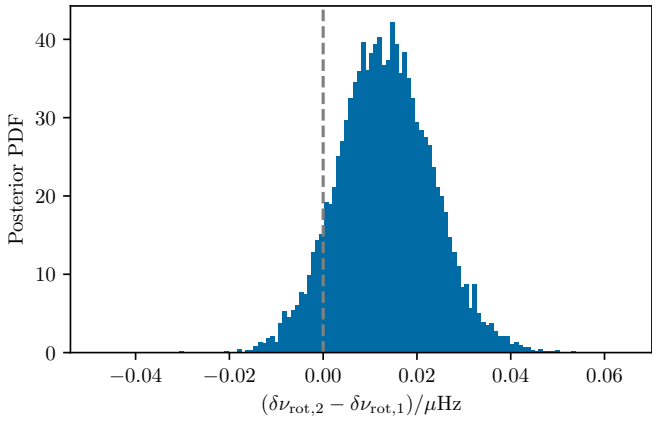

Figure 3. Rough estimate of rotational shear, characterised through the marginal posterior distribution for the difference $\delta\nu_{\mathrm{rot},2} - \delta\nu_{\mathrm{rot},1}$ in the widths of the multiplet splittings for modes of different degree. The distribution can be seen to be a little more than 1σ discrepant with uniform rotation.

For rotation in particular, we find that the averaged $\ell = 1$ and $\ell = 2$ rotational splittings to be $\delta\nu_{\mathrm{rot},1} = 0.091 \pm 0.007$ μHz and $\delta\nu_{\mathrm{rot},2} = 0.104 \pm 0.007$ μHz, with a corresponding pooled inclination of $i_\star = 84^{+4\circ}_{-5}$. Both rotational splittings are larger than the pooled linewidth of $\Gamma = 0.07 \pm 0.01$ μHz. It is thus likely that neither our axial inclination constraint of $i_\star = 84^{+4\circ}_{-5}$, nor our estimates of the rotational splittings themselves, are affected by the systematic biases described in Kamiaka et al. (2018; see also Gehan et al. 2021) in any significant fashion. Moreover, we note that the marginal posterior distribution in the difference between the dipole and quadrupole rotational splittings, which we show in Fig. 3, suggests that they are discrepant from each other, which in turn would indicate spatial variations in the rotation rate. We examine this in more detail in Section B.2.

2.2. *TESS and ASAS-SN Photometry*

In addition to asteroseismology, *Kepler* data suggest that we should in principle also be able to derive photometric surface rotation rates for rotating red giants. The rotational frequencies obtained from our seismic analysis correspond to rotational periods of potentially up to 126 days (from our slower dipole-mode rotational frequency), spanning multiple 27-day sectors. However, the short-cadence PDC-SAP lightcurves from which our asteroseismic analysis above is derived have been aggressively detrended to eliminate long-term temporal variability. As a secondary result of this detrending, discontinuities are also introduced between sectors. In consequence of these, rotational periods longer than 27 days cannot be observed directly from this data product (cf. Avallone et al. 2022). Alternative techniques (e.g. Lu et al. 2020; Claytor et al. 2022) rely on pattern-matching against single sectors and spectroscopic measurements, rather than attempting direct measurement. Given that Zvrk is both rotationally and spectroscopically unusual, and therefore unlikely to be well-described by the training sets of machine-learning pattern matching, we opt to undertake direct measurement instead.

We thus construct our own custom aperture-photometry light curves, correcting for TESS instrumental systematics by applying the pixel-level decorrelation technique (PLD: Deming et al. 2015), as implemented in the `lightkurve` Python package, to the TESS target pixel files. While this suffices to recover slow variability within each TESS sector, the long rotational periods under consideration also require us to stitch TESS sectors together in a principled fashion. Again, since our asteroseismic analysis suggests rotational periods which are far longer than the duration of a single sector, we opt to do this stitching by naive linear extrapolation. Specifically, we fit a linear function to the last 5 days of each sector, and extrapolate the fitted function to the first 5 days of the following sector. The observed flux in the following sector is normalised such that its median flux matches the median value inferred based on the extrapolatation. This procedure is repeated for each consecutive sector. We show the results of this procedure with the blue points in Fig. 4. Note that this procedure relies on there not being gaps between sectors, and so the missing sector 36 in Cycle 3 results in sectors 37-39 not being stitched to the preceding sector 35. Nonetheless, a clear periodic variation can be seen to emerge in Cycle 1, all of whose 13 consecutive sectors are successfully treated with this procedure, with a period of roughly 100 days. Likewise, similar periodicity can be seen in the first 9 consecutive sectors of Cycle 3, albeit at reduced amplitude.

To confirm that these variations are not caused by other latent, unaccounted TESS instrumental systematics, or artificially and inadvertently introduced by these choices of detrending or stitching procedures, we also examined Zvrk through inde-

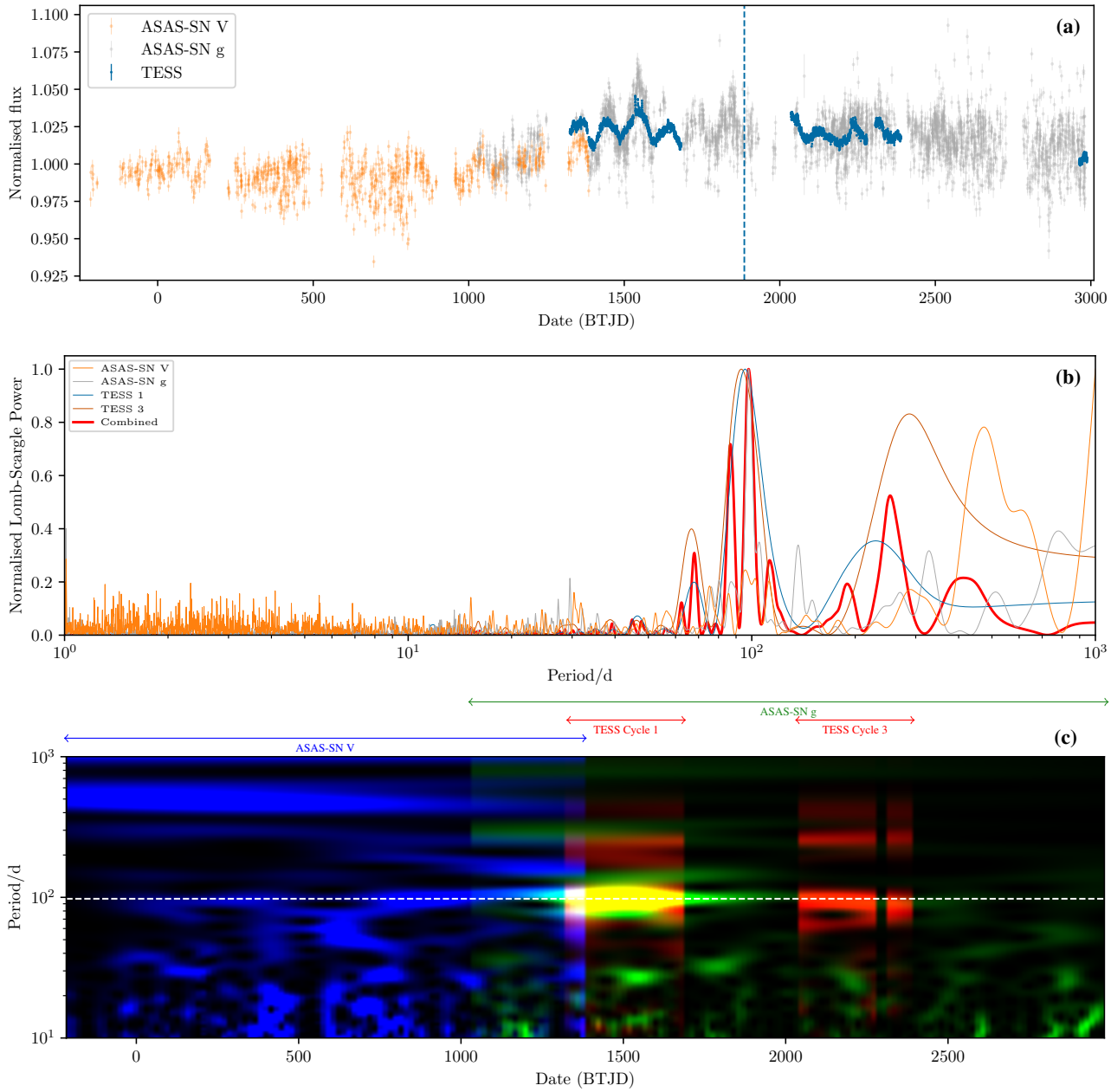

Figure 4. Photometric characterisation of Zvrk. **(a)** Stitched TESS aperture photometry (blue), shown over data from ASAS-SN in *V*-band (orange) and *g*-band (gray). The date of the APOGEE visit is shown with the vertical dashed line. **(b)** Lomb-Scargle power spectral densities from different TESS CVZ cycles and ASAS-SN bandpasses, normalised to give unity at their maximum values. A combined power spectral density incorporating all data sets (having applied offsets shown in panel a) is also shown with the red curve. From the most prominent peak of this combined power spectrum we infer a characteristic period of 99 days. **(c)** Color-separated frequency-time power diagram, with the intensity at each pixel showing the Lomb-Scargle-wavelet-transform power associated with a given time and oscillation period. Different colour channels correspond to different instruments, with TESS shown in red, ASAS-SN g in green, and ASAS-SN V in blue. A nominal oscillation period of 99 days, from our global Lomb-Scargle analysis, is marked out with the horizontal dashed line. An animated version of this panel, to accommodate colourblind readers, is available in the online edition of this paper.

pendent ground-based photometry. We do so by way of the ASAS-SN network of ground-based telescopes (Shappee et al. 2014; Kochanek et al. 2017; Hart et al. 2023). Since Zvrk is fairly bright (with an apparent V magnitude of 10.24), we used aperture photometry with a wider aperture than standard: we construct lightcurves over a 3-pixel-wide aperture, and treat each dither exposure as an independent point in the time series. The residual instrumental systematic perturbations which affect each of the ASAS-SN detectors (aside from lunation and annual variations) remain temporally uncorrelated from those afflicting TESS. Thus, over longer timescales we may still rely on ASAS-SN to anchor our absolute photometric normalisation. We compare in Fig. 4a the normalised ASAS-SN V-band and g-band photometry with our TESS lightcurves, choosing to display each consecutive run of TESS sectors in such a way as to match the median normalisation of the contemporaneous ASAS-SN g-band data points, which as a whole are themselves shown median-normalised. The ASAS-SN V-band data have also been scaled to yield equivalent median normalisation over the overlap period where contemporaneous observations exist with g-band.

The ASAS-SN data exhibit periodicity contemporaneous with that shown in TESS Cycle 1, across multiple cameras, confirming the photometric variations first seen from the TESS data. In the small period of overlap between TESS Cycle 1 and ASAS-SN V-band coverage, the temporal variations in the ASAS-SN data can also be seen to be apparently in phase with the TESS modulation signal. Furthermore, this periodicity can be seen to continue in the ASAS-SN data for at least two more rotational periods after the end of TESS Cycle 1 (i.e. after a BTJD of about 1690), suggesting the persistence of any surface morphology causing the rotational signal.

Many techniques exist for the derivation of the period of this kind of quasiperiodic variability. For our analysis, we rely on the standard Lomb-Scargle technique (e.g. Lomb 1976; Scargle 1982; VanderPlas 2018, and references therein), since it allows us to combine multiple data sets with different temporal sampling characteristics, and has already been used extensively in the literature. We show in Fig. 4b the normalised Lomb-Scargle periodograms for different subsets of the data shown in panel (a), and additionally a periodogram generated from the combined data set, shown with the thick red line. We can see that all of the data sets exhibit a large peak at a period of between 90 to 100 days. Interpreting the combined periodogram as being a log-likelihood function, we use the inverse curvature of this peak (or, equivalently, its half-width) as an estimate of the uncertainty on its location (Ivezić et al. 2014; VanderPlas 2018), and in this fashion find it to be at 99 ± 3 days. The scatter in the location of this peak in the other periodograms shown is 2 days, which we adopt as an estimate of variability between our data sets. To estimate the systematic uncertainty owing to our choice of methodology, we also fit a Gaussian process using a quasiperiodic kernel against the ASAS-SN g-band data set, obtaining a periodicity of 104 ± 7 days. We adopt the discrepancy between the two techniques as an estimate of our systematic error. Thus, we report a rotation rate of $99 \pm 3(\mathrm{stat}) \pm 5(\mathrm{sys})$ days.

The peak-to-peak amplitude of this variability varies between 2-4% depending on the instrument measuring it. The larger amplitude of the modulation as observed by ASAS-SN compared to TESS reinforces an interpretation of this signal as originating from a rotational modulation. A fixed temperature contrast between cool surface features, such as spots or large-scale convective patterns (e.g. Paladini et al. 2018), and the surrounding stellar photosphere, will yield a greater reduction in intensity compared to the rest of the disk when observed in a bluer bandpass than in a redder one, and ASAS-SN's V-band ($\lambda \sim 540$ nm) and g-band ($\lambda \sim 477$ nm) observations are indeed bluer than TESS ($\lambda \sim 787$ nm). If these features are indeed convective in origin, then we should expect them to evolve over the course of the convective turnover timescale. Alternatively, if they arise from near-surface magnetism like that seen in active main-sequence dwarfs, we should also expect their shapes and positions to change over many rotational periods. Either way, this will affect the properties of the observed photometric modulations. The shapes and sizes of such features will affect its amplitude, and their positions will, in the presence of latitudinal differential rotation, modify its apparent period.

The prominence of this photometric rotational signal and, to some extent, its period, do indeed appear to vary over time. The peak of the Lomb-Scargle periodogram for TESS Cycle 1 is located at a period of 96 days, and that of Cycle 3 at 93 days, suggesting some temporal variations in the putative rotational frequency. We investigate this with more detail in Fig. 4c, which shows a frequency-time power diagram generated using the Lomb-Scargle wavelet power spectrum utility function of the ASAS-SN Sky Patrol client (Hart et al. 2023), over which we mark out our nominal surface rotational period of 99 days with a horizontal line. The wavelet-transform power in different bandpasses is shown on this diagram in different colour channels. The normalisation with which each wavelet-transform power is displayed is chosen to saturate each colour channel by a factor of 1.5, to enhance the visibility of lower-amplitude features. The peaks of 100 days in our periodograms in panel (b) correspond to a horizontal band of power on this frequency-time power diagram. Heuristically, the Lomb-Scargle periodograms (up to convolution against a kernel determined by the temporal resolution of this diagram) may be recovered by simply integrating over time. However, for the horizontal band at 99 days, such an integral can be seen to be largely dominated by an episode of large photometric amplitude centred at around BTJD 1500, which, fortuitously, was covered contemporaneously by ASAS-SN g-band, TESS, and (at least at its beginning) ASAS-SN V-band. Moreover, while this rotational peak is substantially less prominent in the ASAS-SN V-band periodogram compared to the others, our wavelet analysis reveals that this is because of time evolution: oscillatory variability at this period can be seen to emerge only after BTJD 700 or so, more than halfway through our temporal coverage in V-band.

2.3. *Spectroscopy*

To further test the interpretation of our quasiperiodic signal as being of rotational origin, we subject Zvrk to the LEOPARD two-component fitting procedure described in Cao & Pinsonneault (2022), applied to an APOGEE spectrum taken during a visit to Zvrk made at MJD 58886 = BTJD 1886, at a time where contemporaneous ASAS-SN g-band coverage indicates the persistence of the photometric modulation signal (vertical line in Fig. 4a). The LEOPARD procedure returns a disk area coverage fraction of $f_{\rm spot} = 0.02$, and a temperature contrast of $x_{\rm spot} = T_{\rm spot}/T_{\rm surf} = 0.8$. Assuming that secondary component corresponds to a single large, morphologically concentrated, surface feature, its coverage fraction and intensity contrast would produce a roughly 2% photometric variability amplitude, which is consistent with that observed in Section 2.2. However, the presence of only a single APOGEE visit prevents us from assessing properties of the evolution of these putative surface features.

In addition to the asteroseismic measurements that we have presented above, spectroscopic measurements of e.g. the stellar metallicity and effective temperature are also necessary as inputs into stellar modelling for more precise constraints on stellar properties. Such measurements for Zvrk already exist in the APOGEE DR17 catalogue (Abdurro'uf et al. 2022, wherein it is found as 2MASS ID 05592585-5911542), derived from the spectrum taken during its single APOGEE visit. Zvrk's fitted effective temperature from DR17 is $T_{\rm eff} = 4320 \pm 80$ K, and its metallicity is $[{\rm M/H}] = -0.21 \pm 0.08$ dex. This value of the effective temperature, in conjunction with the solar-calibrated scaling relation $\nu_{\rm max} \sim g/T_{\rm eff}$, yields $\log g_{\rm seis} = 1.76 \pm 0.03$, which is significantly lower than the APOGEE DR17 reported value of 2.11 ± 0.08 dex. In principle, as is often done in other works combining asteroseismology with spectroscopy, we may employ our asteroseismic measurement of $\log g$ as a direct constraint on the surface gravity, and iterate between fitting for the remaining quantities with it held fixed, and refining asteroseismic $\log g$, until the fitted values converge. However, this iterative procedure is typically performed with far more precise constraints on $\nu_{\rm max}$ than we have available here. Conversely, using our asteroseismic surface gravity here does not significantly modify the fitted temperature and metallicity. We therefore adopt the nominal APOGEE values for $T_{\rm eff}$ and metallicity, and their uncertainties, in our subsequent analysis. We may then estimate a spectroscopic rotational broadening $V \sin i$ through the differential Doppler-broadening technique also used in Tayar et al. (2022), which estimates the optimal amount of additional broadening required to reconcile a spectral template (given values of $T_{\rm eff}$, $\log g$, and abundances) compared with the observed APOGEE spectrum. This procedure is sensitive to the adopted value of the surface gravity, as it determines the amount of pressure broadening in the template spectrum, which is highly degenerate with the fitted rotational broadening (cf. Thompson et al. 2019). Holding $\log g$ fixed at its seismic value for this purpose, we obtain that $V \sin i = 10.1 \pm 0.7$ kms^{-1}. Conversely, this rotation is likely the cause of the offset we obtain between our seismic surface gravity, and the fitted spectroscopic value in DR17.

Several spectral features which are also important to our analysis — specifically, pertaining to Zvrk's Hα (Fig. 5a) and lithium (Fig. 5b) absorption features — lie at optical frequencies, outside of APOGEE's near-IR coverage. Thus, in addition to APOGEE spectra, we also obtained a high-resolution GALAH spectrum covering these optical frequencies, from which a similar template-fitting procedure yields $\log g = 1.7 \pm 0.2$ dex, $T_{\rm eff} = 4250 \pm 100$ K, $V \sin i = 9.5 \pm 1.0$ kms^{-1}, and $[{\rm Fe/H}] = -0.36 \pm 0.10$ dex. Since these values are not significantly different from those returned from APOGEE DR17, we adopt the APOGEE values in our asteroseismic analysis, so as to minimise systematic discrepancies between our derived seismic quantities and, e.g., those previously determined for members of the APOKASC sample (Serenelli et al. 2017; Pinsonneault et al. 2018, in prep.). Nonetheless, the GALAH spectrum will be critical for our subsequent abundance analysis.

2.4. *What is Zvrk?*

Our preceding asteroseismic analysis — specifically, the detection of solar-like oscillations at all, and the low associated value of $\Delta\nu$ — favours an interpretation of Zvrk as being a first-ascent red giant. However, its combination of high surface rotation, strong lithium absorption line, and low mean density may also be compatible with it being a pre-main-sequence T Tauri star. Were Zvrk actually to be a T Tauri star, we should also expect to see strong Hα line emission in its spectrum originating from an extensive circumstellar disk, with substantial amounts of ionised hydrogen present. Contrary to this, Zvrk's Hα line, measured with GALAH, can be seen to be a very deep absorption feature (Fig. 5a), comparable to other red giants (both first-ascent and core-helium-burning), rather than the emission expected of T Tauri stars. Morever, occultation by circumstellar material tends to produce irregular photometric variability with a characteristic "dipping" pattern, as opposed to the quasiperiodic variability shown in Section 2.2. In any case, the modulation amplitude of a few percent that we measure in Section 2.2, using multiple instruments, is also an order of magnitude smaller than that typically produced by such occultation.

Hα absorption and low photometric amplitudes do not entirely rule out Zvrk being a T Tauri star, as certain "weak-lined" T Tauri stars are known to exist, which lack significant disks, and, therefore, Hα emission. However, were Zvrk actually to be a weak-lined T Tauri star, its dynamics would also be extremely anomalous. While rapid for a red giant, Zvrk rotates an order of magnitude more slowly than essentially all rotational measurements of weak-lined T Tauri stars in the catalogue of Bouvier et al. (2016). A comparably slowly rotating T Tauri star would therefore have to be much younger than their sample, drawn from NGC 2264 at 3 Myr old. This is also suggested by Zvrk's surface gravity, which is much lower than typical for a T Tauri star. However, Zvrk's lithium equivalent width of 100 mÅ is lower than that of the NGC

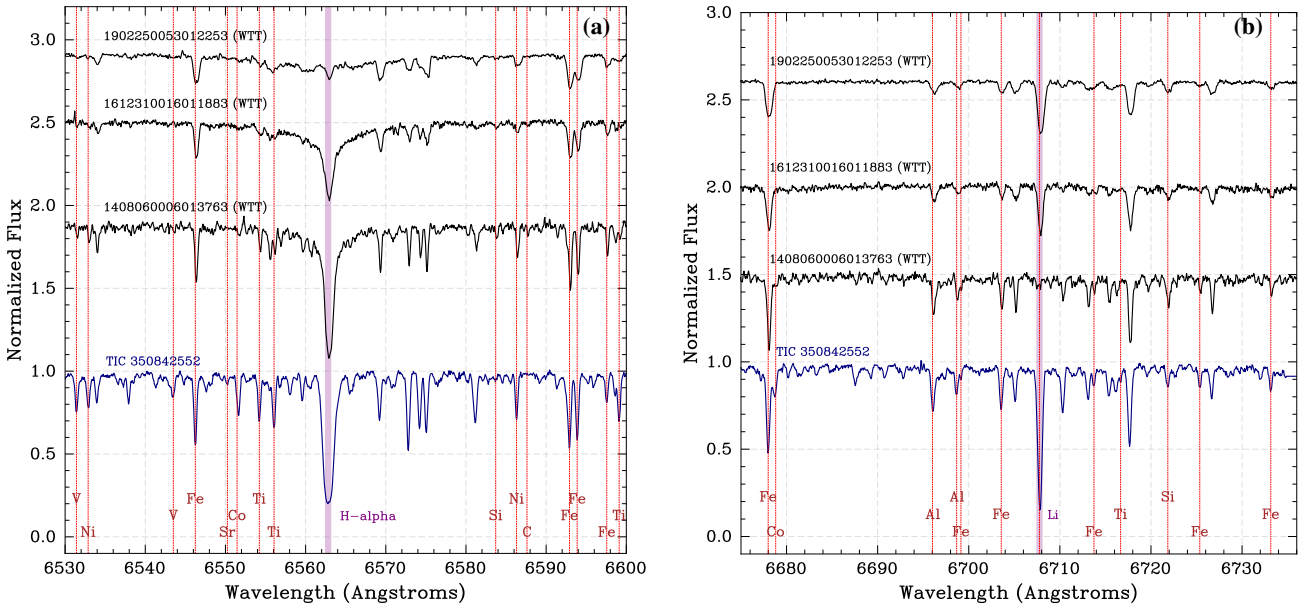

Figure 5. Excerpts of high-resolution GALAH spectra, showing **(a)** Hα, and **(b)** lithium absorption features. Zvrk's spectrum is shown with the blue solid curve, while comparisons with weak-lined T Tauri stars from Xing (2010) are shown in black.

2264 sample, rather than higher as we would expect from a younger object. The only candidate weak-lined T Tauri star of comparable rotational period and lithium abundance that we were able to find in the literature, V501 Aur, was later shown to be actually a misclassified red giant (Vaňko et al. 2017).

Since T Tauri stars are also known to be preferentially associated with natal comoving groups, such a young object would be likely found close by to other comoving objects. However, using the `Comove` software package (Kraus & Rizzuto 2022), we are unable to find any co-moving sources (i.e. with systemic velocities within 5 km s^{-1} of Zvrk's) within a 25 pc search radius centred on Zvrk in the Gaia DR3 catalogue. Thus, in addition to being weak-lined, and both rotationally and chemically unusual, Zvrk would also have to be kinematically anomalous for consistency with being a T Tauri star.

As such, although its chemical and rotational properties would make Zvrk an unusual red giant, our above discussion suggests it would be an even more unusual T Tauri star. Accordingly, we will proceed in our following analysis on the assumption that Zvrk is indeed a first-ascent red giant.

3. DERIVED STELLAR PROPERTIES

3.1. *Detailed Asteroseismic Modelling*

Given the global asteroseismic properties $\Delta\nu$ and $\nu_{\rm max}$, and our spectroscopic effective temperature, the so-called "direct method" inverts their usual scaling relations to produce mass and radius estimates. We do so in a similar fashion to the APOKASC3 catalogue of solar-like oscillators (Pinsonneault et al. in prep.) in the APOGEE DR17 sample, including incorporating a structural correction factor $f_{\Delta\nu} = 0.97$ via the prescription of Sharma et al. (2016), and obtain for Zvrk that $M_\star = (1.181 \pm 0.15) M_\odot$, $R_\star = (23.7 \pm 1.1) R_\odot$.

The uncertainties on these estimates are large, both owing to the fact that $\nu_{\rm max}$ is difficult to measure for evolved stars with comparatively few visible modes, as well as owing to the fact that the scaling relations themselves may not be reliable at advanced stages of evolution (whence the need for ad-hoc corrections like $f_{\Delta\nu}$ in the first place). However, these are still helpful in bounding the parameter space for further analysis. To refine our estimates of stellar properties, we turn to detailed modelling of stellar structure, as constrained by our measurements of individual mode frequencies. Having constrained Zvrk's structure, we will then examine the internal stratification of rotation in its envelope, by generalising existing rotational inversion techniques.

Table 1. Global properties adopted in stellar modelling.

Constraint	Value	Reference
$T_{\rm eff}$ / K	4320 ± 80	Abdurro'uf et al. (2022)
[M/H]	-0.21 ± 0.08	Abdurro'uf et al. (2022)
$L/L_\odot$	174 ± 10	Gaia Collaboration et al. (2018)
$\Delta\nu/\mu$Hz	1.21 ± 0.01	This work
$\nu_{\rm max}/\mu$Hz	7.5 ± 0.3	This work

For the purposes of detailed seismic modelling, we rely on the implied $m = 0$ mode frequencies from the MCMC procedure that we described in Section 2.1, which we list in full in Table A1 in the appendix. Supplementing these mode frequencies are constraints on some global stellar properties,

which we list in Table 1. Using these, we search for stellar models which match the global properties and individual mode frequencies by minimising the sum-of-squares discrepancy function, where for a given stellar model described by parameters θ we have

$$\chi^2_{\rm tot}(\theta) = \left(\frac{T_{\rm eff}(\theta) - T_{\rm eff\,obs}}{\sigma_{T_{\rm eff}}}\right)^2 + \left(\frac{[{\rm M/H}](\theta) - [{\rm M/H}]_{\rm obs}}{\sigma_{[{\rm M/H}]}}\right)^2 + \left(\frac{L(\theta) - L_{\rm obs}}{\sigma_L}\right)^2 + \chi^2_{\rm seis}(\theta), \quad (4)$$

where $\chi^2_{\rm seis}$ is a cost function incorporating constraints from the individual mode frequencies. The precise form of it will depend on how we should choose to correct for systematic errors in the near-surface physics of our stellar models (the asteroseismic "surface term"). For this exercise, we tested both the parametric surface-term correction of Ball & Gizon (2014), and the nonparametric surface-insensitive penalty function of Roxburgh (2016). We find, however, that our results do not change significantly between the two. To be conservative, we report results obtained with the latter, which provides slightly larger uncertainties (Ong et al. 2021).

Importantly, we note that neither $\Delta\nu$ nor $\nu_{\rm max}$ enter directly into the constraints derived in this fashion: for this exercise, they affect only ancillary properties of our search for best-fitting parameters $\theta = (M_\star, Y_0, Z_0, \alpha_{\rm MLT}, t)$. In particular, we search for stellar models using the differential-evolution optimisation scheme, as implemented in Mier (2017), which requires us to supply bounds on our search space. Based on our scaling-relation estimate for the seismic mass, we restrict our attention to $M_\star/M_\odot \in [1.05, 1.3]$; we also restrict our attention to stellar models within ±25% of our adopted value of $\nu_{\rm max}$, as a proxy for evolution up the RGB. For the remainder of our parameters, we adopt fairly large bounds of $Y_0 \in [0.248, 0.32]$, $Z_0 \in [0.008, 0.02]$, and $\alpha_{\rm MLT} \in [1.7, 2.1]$.

For each trial θ, we generate an evolutionary track of stellar models using MESA r12778, using the chemical mixture of Grevesse & Sauval (1998). Stellar models were generated without overshooting or mass loss, and with an Eddington-gray model atmosphere. While we include the effects of the diffusion and settling of helium and heavy elements, we vary the overall mixing coefficient as a function of stellar mass according to the prescription of Viani et al. (2018), in order to smoothly disable it at masses substantially higher than 1.25 $M_\odot$. For models on each evolutionary track that lie within our permitted range of $\nu_{\rm max}$ values, we compute the radial p-mode frequencies, and those of the nonradial π modes as isolated using the prescription of Ong & Basu (2020), with the GYRE stellar oscillation solver. We then run 400 iterations of the differential evolution optimisation algorithm, retaining all stellar models generated along the optimisation trajectory.

From optimisation, we obtain a best-fitting point estimate of $\hat{\theta}_{\rm MLE} = (1.18 M_\odot, 0.289, 0.0099, 1.863, 4.7\ {\rm Gyr})$. We will use this best-fitting model, and its associated evolutionary track, in our subsequent analysis requiring knowledge of Zvrk's temporal evolution or interior structure. More generally, in order to report uncertainties, we treat all of the models generated over the course of performing such optimisation as a set of nonuniform samples over our parameter space, $\Theta = \{\theta_i\} = \{(M_i, Y_{0,i}, Z_{0,i}, \alpha_{{\rm MLT}i}, t_i)\}$. Associated with this set of samples are the values of a likelihood function defined through Eq. (4) as $\mathcal{L}(\theta_i) = \exp[-\chi^2_{\rm tot}(\theta_i)/2]$, evaluated for all $\theta_i \in \Theta$. If we were to compute likelihood-weighted averages and quantiles of stellar properties with respect to Θ, as is often done with grid-based modelling (e.g. Cunha et al. 2021), we would effectively be providing Bayesian posterior estimates of these properties and their uncertainties, with the prior distribution determined by the sampling function over Θ.

Such a procedure would yield estimates with respect to a uniform prior when used in grid-based modelling, where Θ is sampled uniformly (typically using a discretised coordinate mesh or Sobol sequence). In our case, however, the sampling over Θ is determined by our optimisation trajectory, which becomes increasingly densely sampled in the neighbourhood of the best-fitting point. Thus, a naive likelihood-weighted average would be prior-dominated in such a fashion as to both artificially select for the best-fitting result, and also systematically reduce the estimated uncertainties around it. Instead, it would be preferable for us to also return posterior estimates with respect to an uninformative, uniform prior over our input parameters, and to do this we must divide out the sampling function over Θ. We estimate the sampling function $s(\theta)$ over Θ using a kernel density estimator, and compute weighted quantiles with respect to modified likelihood weights $w_i \propto \mathcal{L}(\theta_i)/s(\theta_i)$, with normalisation chosen to set $\sum_i w_i = 1$. We report the resulting posterior medians and $\pm 1\sigma$ quantiles for our input parameters, and Zvrk's radius, in Table 2. In addition, we provide values from a solar-calibrated model for comparison, where applicable.

Table 2. Global properties returned from stellar modelling with mode frequencies.

Quantity	Inferred Value	Remarks
$M_\star/M_\odot$	$1.14^{+0.05}_{-0.03}$	—
$R_\star/R_\odot$	$23.5^{+0.4}_{-0.2}$	—
$\alpha_{\rm MLT}$	$1.89^{+0.12}_{-0.08}$	$\alpha_\odot = 1.824$
Y_0	$0.273^{+0.03}_{-0.02}$	$Y_\odot = 0.268$
Z_0	0.010 ± 0.001	$Z_\odot = 0.018$
Model age/Gyr	$5.4^{+1.0}_{-0.8}$	Single-star Scenario

As we might expect, the stellar properties that emerge from our detailed modelling are far more precise than, although still consistent with, the rough estimates obtained from scaling relations. Given this constraint on the stellar radius, and using our posterior median estimate of the stellar inclination, our spectroscopic rotational broadening implies a surface rotation

rate of $\Omega_{\rm surf}/2\pi = 0.099 \pm 0.007 \mu$Hz, which lies between the values that we obtain from the dipole and the quadrupole rotational splittings.

Finally, we consider systematic errors induced by variations on the techniques used for detailed modelling, which have been shown to be nontrivial for grid-based modelling of red giants (e.g. Campante et al. 2023). We conducted a separate optimisation-based modelling exercise, with stellar models generated using MESA r15140, without diffusion and settling of helium and heavy elements, using a constant opacity in the atmosphere rather than the Eddington $T-\tau$ relation, and with the chemical mixture of Asplund et al. (2009). The mass-loss prescription of Reimers (1975) was also used, with an efficiency parameter of $\eta = 0.1$. For this exercise, only radial mode frequencies were incorporated into the asteroseismic constraint; these were computed from stellar models using the `ADIPLS` oscillation solver, and included in the penalty function Eq. (4) through the surface-term correction of Ball & Gizon (2014). A search for the best-fitting parameters was conducted via the `astero` module of MESA, using the Nelder-Meade optimisation scheme, and with uncertainties estimated using a local Jacobian matrix evaluated by finite differencing on a bounding simplex around the best-fitting sampled value. This second optimisation exercise yields an estimate for the initial mass of $1.142 \pm 0.050 M_\odot$ and a present mass of $1.138 \pm 0.050 M_\odot$, as well as an estimated radius of $23.44 \pm 0.11 R_\odot$; these are consistent with the values that we have reported in Table 2. Any systematic differences between the initial and final mass, as well as between these results and those reported in Table 2, are clearly dominated by the much larger statistical uncertainties. Since the values in Table 2 include constraints from nonradial modes, we adopt them as our preferred values for subsequent analysis. We also adopt the best-fitting MESA model from this optimisation exercise as a point estimate of Zvrk's interior structure, which we will use in subsequent analysis.

3.2. *Abundance Analysis*

Our use of almost the same methods for deriving a seismic-scaling-relation mass and radius as the APOKASC3 catalogue (Pinsonneault et al. in prep.) allows us to perform an apples-to-apples comparison of Zvrk's scaling-relation mass, and carbon-to-nitrogen ratio [C/N] $= -0.08 \pm 0.017$(stat) $\pm$ 0.057(sys) from the APOGEE DR17 catalogue, to the mass-enrichment sequence of the APOKASC3 sample. We show this comparison in Fig. 6, restricting this comparison to only first-ascent red giants, and to stars with with metallicities within 0.1 dex of Zvrk's.

In the background of Fig. 6, a clear mass-enrichment sequence can be seen, as marked out by the dark region of histogram bins. This is because both the central stellar temperature, and the main-sequence convective core mass, are tightly correlated with the total stellar mass. As a result of the former, the strong sensitivity of the CNO cycle to the reaction temperature causes a larger proportion of the main-sequence nuclear processing of hydrogen to be performed through the CNO cycle as the stellar mass increases; as a result of the latter, a larger reservoir of hydrogen is available to predominantly CNO-cycle burning in more massive stars. At core hydrogen exhaustion, more massive stars will therefore have larger residual quantities of unreacted ^{14}N (from the rate-limiting proton-capture reaction in the CNO cycle) present in their cores, which is then redistributed into the envelope during first dredge-up. Correspondingly, we would expect — within a limited range of metallicities, as we have considered here — that the carbon-to-nitrogen ratio [C/N] should be tightly, and negatively, correlated with the stellar mass.

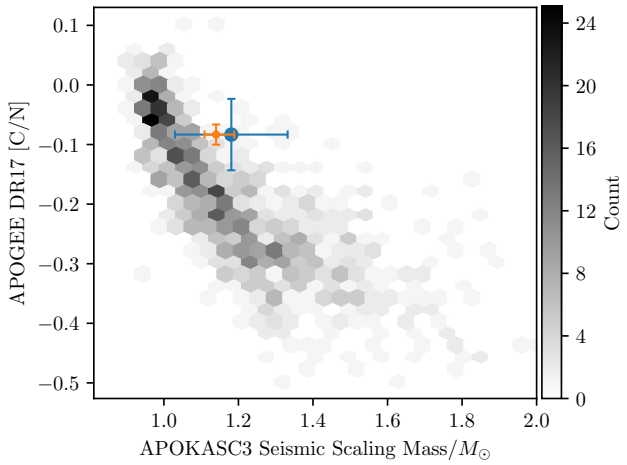

Figure 6. APOGEE DR17 [C/N] of Zvrk relative to APOKASC3 observational sample, with a metallicity cut of 0.1 dex around the nominal value for Zvrk, and restricting attention to only first-ascent red giant stars (per the identification supplied by APOKASC3). A well-defined mass-enrichment sequence can be seen. Zvrk can be seen to lie above this enrichment sequence, given its seismic mass and relative abundances. We plot the location of Zvrk on this diagram using both its scaling-relation mass (blue) and total uncertainty in [C/N], for an apples-to-apples comparison against the scaling-relation masses in the APOKASC3 catalogue, but also show its seismic mass constrained by detailed modelling against individual mode frequencies, and statistical error in [C/N] (orange), to indicate our actual precision of relative inference.

Zvrk can be seen on Fig. 6 to lie above this mass-enrichment sequence (blue point). While the uncertainties on both the scaling-relation seismic mass and on the [C/N] measurement are large enough that this departure is only weakly suggestive, we note that detailed modelling against individual mode frequencies constrains the seismic mass far more precisely than scaling relations can; we describe our derivation of such a mass estimate in more detail in Section 3.1. Moreover, since the sample of [C/N] measurements is instrumentally and methodologically homogenous, the relevant systematic error for an intra-sample comparison of this kind should be smaller than the empirical absolute calibration of Hayes et al. (2022) that we have quoted above. We illustrate the detailed-modelling mass, accompanied by statistical uncertainties on

[C/N], with the orange data point. Were the systematic offsets between the detailed-modelling and scaling-relation seismic masses to be small, the former would more strongly disfavour Zvrk lying on the APOKASC mass-enrichment sequence. Given the above discussion, this would in turn suggest that the material in Zvrk's convective envelope is less nuclear-processed than would be typical for an ordinary red giant of comparable mass and radius. However, our only avenue for an apples-to-apples comparison is through our unfortunately imprecise scaling-relation mass, since only scaling-relation and not detailed-modelling seismic masses are available (and for that matter, feasible) for all the rest of the APOKASC3 catalogue. Hence, we are unable to definitively assess if Zvrk's departure from the enrichment-mass sequence is more than 1σ-significant, as our scaling-relation mass appears to suggest.

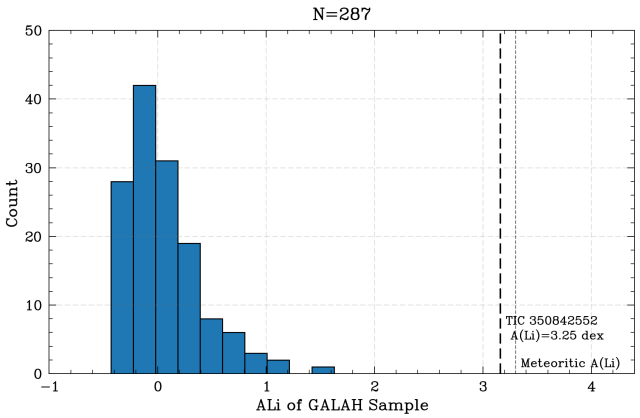

Figure 7. Comparison of Zvrk's lithium abundance, shown with the dashed line, against the general population described by a control sample of GALAH stars — chosen by way of colour, magnitude, metallicity, and Gaia RUWE cuts — of whose lithium abundance measurements a histogram is plotted with the blue bars.

Finally, we recall that our initial selection of Zvrk was on the basis of a measurement of enhanced lithium enrichment, which we measure to be A(Li) = 3.16 ± 0.08 dex — almost meteoritic — by combining a measurement of [Fe/H] from APOGEE DR17, [Li/Fe] from GALAH DR4, and the solar value of A(Li) = 0.96 ± 0.05 dex of Wang et al. (2021). To assess the statistical significance of this measurement, we compare this value to those obtained from comparable stars in the GALAH sample. Specifically, we consider A(Li) measurements of stars whose reddening-corrected Gaia BP – RP colours were within 1σ of Zvrk's, whose GALAH [Fe/H] values were within 0.1 dex of Zvrk's APOGEE DR17 value of 0.24, whose Gaia absolute magnitudes were within 1σ of Zvrk's, and whose Gaia DR3 Renormalised Unit Weight Errors (RUWE) were less than 1.4, to select single stars (1.4 being the typically quoted threshold value indicating the presence of an unresolved binary inducing photocentre jitter: Rizzuto et al. 2018). This yielded a subsample of 287 stars, a histogram of whose A(Li) measurements we show in Fig. 7. This control sample population has a median A(Li) of −0.02 dex and a MAD of 0.2 dex, which is consistent with (if a little lower than) the baseline estimate provided in Soares-Furtado et al. (2021). Zvrk's lithium enrichment, indicated with the vertical dashed line, is clearly far higher than of this control sample.

A high lithium abundance is customarily attributed to mass transfer or tidal interactions owing to a binary companion, or potentially its engulfment. Since only one APOGEE visit to Zvrk was performed, we are unable to determine the properties of any unresolved orbital companion from the time evolution of its APOGEE radial velocities. However, Zvrk has a Gaia DR3 RUWE of 1.056, close to unity, which indicates that such an unresolved companion, or at least one in an orbital configuration that might induce photocentre jitter, is unlikely to be present. Moreover, any undetected companion must produce a radial velocity (RV) signal consistent with or less than the observed RMS RV scatter of $\sigma_v = 0.16$ km/s. We discuss such a putative companion in more detail below, in Section 4.1.

Zvrk is also not present in the RRRG catalogue of Patton et al. (2023), which identifies rapid rotators based primarily on their fitted temperatures being anomalously cool relative to the APOGEE DR16 catalogue. This suggests that, even if Zvrk's present rotational configuration should have been produced as a result of some kind of impulsive event causing it to puff up, such a structural perturbation should have thermally relaxed by now. Thus, at least Zvrk's structure, although probably not its evolutionary history, should be amenable to description by numerical stellar models in hydrostatic equilibrium, as we have assumed.

3.3. *Rotation*

Our different values of the rotational splitting as fitted against dipole vs. quadrupole modes (e.g. Fig. 3) suggests the existence of radial differential rotation. In less evolved stars, p-mode asteroseismology has been used to place constraints on this through so-called "rotational inversion" techniques (e.g. Schunker et al. 2016a,b; Eggenberger et al. 2019a). Since per-multiplet rotational splittings, as ordinarily required by these methods, could not be reliably constrained for Zvrk, we instead generalise existing techniques for this problem to operate on the power spectrum directly, rather than on lists of fitted multiplet splittings. We describe our approach more fully in Appendix B, and specifically report numerical results in Section B.2.

We show a summary of our consolidated constraints on Zvrk's rotational configuration in Fig. 8. The purely asteroseismic constraints that we derive in Section B.2 are shown in blue and orange, while our two measurements of the surface rotation rate — from photometric modulations, and from combining Doppler line broadening with our asteroseismic inclination and model radius — are shown in gray. As far as radial differential rotation is concerned, we may conclude from the available asteroseismic data only that (1) rotational shear is

likely to be present in Zvrk's convective envelope, but (2) both senses of rotational shear, in bulk, are permitted by such constraints as we are able to produce. (3) Under both scenarios, there is some location in Zvrk such that the local rotational gradient is in the sense of Ω increasing outwards. If the bulk shear is such that Ω decreases outwards, then a secondary, very thin, shear layer near Zvrk's surface produces consistency with the observed photometric rotation rate. If the bulk shear is such that Ω increases outwards, this shear may happen over longer length scales, and be situated closer to the interior.

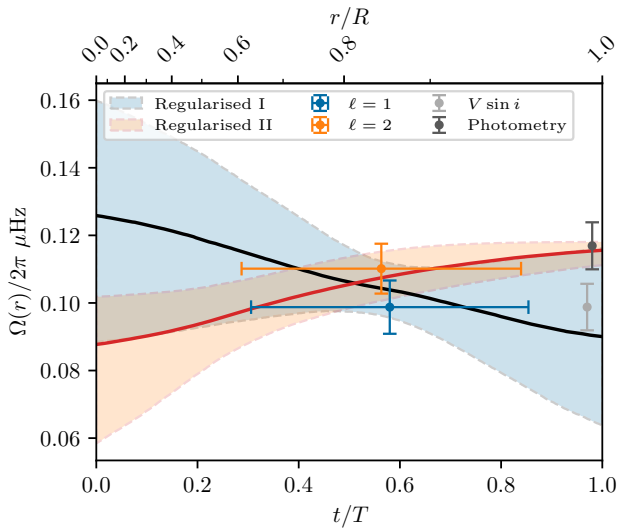

Figure 8. Summary of various rotational measurements, displayed with respect to both the acoustic radial coordinate t, and physical radius r. Median rotational profiles from both of our regularised exercises in Fig. B3 are shown with the solid lines, and their credible regions with the filled areas. The rotation rates from the pooled localisation kernels, and their localisation widths, are indicated with the two coloured data points. Our two estimates of the surface rotation rate (from photometry, and by combining spectroscopic $V \sin i$ with asteroseismic inclination and a radius from stellar modelling) are indicated with the gray data points.

While both of our direct measurements for the surface rotation rate sit slightly higher than our unconstrained regularised predictions for the surface rotation rate from asteroseismology (blue shaded region), we note that the discrepancy between the two direct measurements is greater than between either of the two, and our asteroseismic prediction. As we discuss in Section B.2, an ad-hoc combination of anti-solar latitudinal differential rotation and high-latitude spotting could bring the equatorial surface rotation rate implied by photometry into agreement with our asteroseismic measurements of the bulk rotation rate in the envelope. Conversely, in the more likely scenario of low-latitude features and solar-like latitudinal differential rotation, our photometric value would be more representative of an equatorial rotation rate than the value produced by Doppler line-broadening, which is integrated over the visible disk.

Our somewhat loose constraints on Zvrk's rotational stratification have unfortunate implications for ongoing attempts to make similar measurements for less evolved red giants using existing TESS data. As we have discussed, disentangling p-mode rotation rates from the observed mixed modes in these red giants remains an open problem. Nonetheless, our results suggest that even if this methodological barrier were to be surmounted, one would still need both more precise constraints on the multiplet rotational splittings, and more available multiplets with precisely measurable rotational splittings, than we have at our disposal here, in order to place well-defined constraints on envelope rotational shear. Conversely, this also highlights the pressing need for far more precise measurements on rotational splittings, which will only be possible with qualitatively longer time series, than we have at our disposal.

4. DISCUSSION

4.1. *Formation and Mass Constraints*

Since we have only measured Zvrk's present state (with other initial conditions being inferred from modelling), any discussion about how its rotational and chemical configuration came to be must necessarily be speculative to some extent. However, we identify four (mutually nonexclusive) classes of explanations for it, which would roughly yield both a high rotation rate, and an enhanced lithium abundance:

(I) First, for the sake of argument, Zvrk could represent significant departures from the existing theory of single-star evolution. To match its fast rotation rate, its evolution would necessitate an efficiency of angular momentum transport, and correspondingly chemical mixing, far in excess of that currently assumed of red giants.

(II) Alternatively, interactions with an orbiting companion would yield enhanced lithium at Zvrk's surface. In this scenario, its high rate of rotation could be attributed to tidal spin-up as a result of binary interactions. Such spin-up might also induce additional episodic mixing, such through rotational shear or the Cameron-Fowler mechanism (Cameron & Fowler 1971), thereby causing self-pollution of lithium into the envelope.

(III) An orbiting companion overfilling its Roche lobe could instead give rise to mass transfer, with the accreted material directly depositing angular momentum into Zvrk's envelope. This material would also enrich Zvrk's envelope in lithium if the companion were to be a sufficiently hot main-sequence star, or conversely insufficiently massive to begin breaking down its initial lithium content.

(IV) Finally, both the enhanced lithium abundance and high rate of rotation could be attributed to Zvrk having engulfed at least one formerly orbiting companion (e.g. Stephan et al. 2020; O'Connor et al. 2023), with both matter and angular momentum being directly deposited

into its envelope, and being redistributed over the course of several mixing timescales.

On the face of it, scenario (I) ought to cause Zvrk to become anomalously ^{14}N-rich relative to the APOGEE [C/N] mass-enrichment sequence, and hence its actual position in Fig. 6 renders this hypothesis unlikely. Moreover, even unphysically efficient post-main-sequence angular momentum transport from the core into the envelope cannot replace the total angular momentum lost on the main sequence to magnetic braking, and — as we discuss in Section 4.3 — even in the absence of magnetic braking, Zvrk must have been rotating very fast (half the breakup rate) on the main sequence in order to produce its present angular momentum. Likewise, were accretion under scenario (III) to be ongoing, we would expect that it should happen through an accretion disk, detectable in spectroscopy by Hα emission, if ionised hydrogen were to be accreted, or more generally through an infrared excess. As we note in Section 2.4, we do not detect the former. The latter is expected to manifest as excess colours derived from the Wide-field Infrared Survey Explorer's (Wright et al. 2010) photometric bandpasses with central wavelengths of 3 (W_1), 4.5 (W_1), 12 (W_3), and 22 μm (W_4). Zvrk's measured values of $W_1 = 7.06 \pm 0.05$, $W_2 = 7.18 \pm 0.02$, $W_3 = 7.06 \pm 0.02$, and $W_4 = 6.99 \pm 0.06$, yield color excesses that either are consistent with zero (e.g., $W_1 - W_3$) or are far below typical detection thresholds of infrared excess (e.g. Rizzuto et al. 2011; Nikutta et al. 2014; Bromley et al. 2021; Martell et al. 2021). This suggests that even were accretion onto Zvrk to have occurred historically, this must have stopped by now, potentially ending with the tidal disruption and engulfment of the donor. Thus, scenarios (I) and (III) are likely not viable in isolation.

Regarding scenario (II), let us first consider the possibility of a currently undetected companion, orbiting in a stable configuration, being the sole cause of Zvrk's unusual properties. While Zvrk's low Gaia RUWE value disfavours the presence of a stellar-mass orbital companion massive and widely-separated enough to perturb its photocentre over the existing temporal baseline, this does not exclude a lower-mass companion, which would also have to be closer in in order to induce any chemical or rotational anomalies. However, such a close-in companion would potentially induce large orbital RVs. RV constraints from Gaia in turn allow us to place limits on allowable combinations of masses and orbital separations. Specifically, at an orbit with semimajor axis a, a companion of mass m_p would produce a radial velocity semiamplitude of

$$K = m \sin i_p \sqrt{\frac{G}{Ma(1-e^2)}}, \tag{5}$$

which we express in terms of the total and reduced masses

$$M = M_\star + m_p; m = \frac{M_\star m_p}{M_\star + m_p}. \tag{6}$$

If Zvrk were to have been spun up by tidal torques exerted by this companion, its rotation would have to be aligned with the orbital angular momentum, and so our asteroseismic analysis demands $\sin i_p = \sin i_\star \sim 1$. From Eq. (5), one may estimate minimal RMS RV variations Σ given an observing duration; e.g. $\Sigma \to K/\sqrt{2}$ for baselines longer than the orbital period. Compared to this, the Gaia DR3 RMS RV scatter of $\sigma_v = 0.16$ km/s, over a 2.2-year time baseline in which $N = 16$ measurements have been taken, would rule out minimal RMS variations Σ larger than σ_v. This constraint then defines the boundary of those combinations of companion mass and orbital separations ruled out by Gaia, shown with the red curve in Fig. 9: the red shaded region above it is excluded by Gaia RVs.

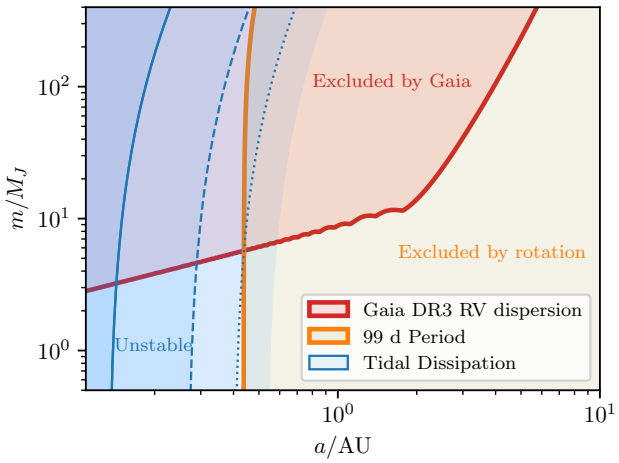

Figure 9. Constraints on allowable combinations of undetected companion masses and orbital separations. Shading shows regions excluded by various constraints, with the boundaries of these regions marked out with various curves. The red solid curve, and shaded area above it, shows combinations excluded by the Gaia DR3 RV dispersion. The orange solid curve, and the shaded region to its right, shows combinations which would achieve tidal locking with Zvrk before being able to spin its envelope up to a 99-day rotational period, and are therefore excluded by the detection of such a signal. The blue curves, and shaded regions to their left, show the loci at which the effective radius of Zvrk's Roche lobe are equal to (solid curve), twice (dashed curve), and three times (dotted curve) the asteroseismic radius. The resulting large tidal bulge would lead to significant orbital decay. All combinations of companion mass and orbital separation can be seen either to be excluded by observational constraints, or to lead eventually to inspiral and engulfment.

Under scenario (II), Zvrk's 99-day rotational signal would also have to be explained by this companion, which would further exclude other regions of this parameter space. In particular, were Zvrk to have been spun up by tidal interactions alone, its final rotational frequency would be bounded from above by the companion's orbital frequency, since the torque acting on Zvrk would disappear upon tidal locking. As such, our rotational signal demands that such an orbital companion be closely separated: it cannot have an orbital period much larger than 99 d. Combinations of m and a with the Keplerian orbital

velocity equal to 99 d are shown in Fig. 9 in orange: the orange shaded region to its right is excluded by Zvrk's rotation.

What remains is a small window of the parameter space, with $a \lesssim 0.4$ au and $m \lesssim 5 M_J$. However, such orbital configurations are liable to be unstable. In particular, we show with the blue curves in Fig. 9 the combinations of m and a such that the effective spherical radius of Zvrk's Roche lobe in such a binary system, computed using the prescription of Eggleton (1983), is equal to (solid curve), twice (dashed curve), and three times (dotted curve) our constraint on Zvrk's asteroseismic radius. Were Zvrk to take up such a substantial fraction of its Roche lobe (blue shaded region) in this binary configuration, the tidal bulge raised on it would be large, and the resulting orbital decay would cause its companion to spiral inwards, eventually to be engulfed. All these suggest that scenario (II) alone might not describe Zvrk's present configuration. Conversely, any orbital configuration in scenario (II) consistent with both the rotational and velocimetric constraints above would require us to consider scenario (IV) anyway.

If we assume that Zvrk's rapid rotation is primarily caused by the engulfment of a planetary companion in scenario (IV), we can use the angular momentum of its envelope's rotation to estimate the mass and orbital properties of such a planet. For simplicity we assume that the currently observed angular momentum of the envelope stems purely from the engulfed object, as stellar expansion and magnetic braking should have significantly reduced the primordial angular momentum of the star (which we discuss in more detail in Section 4.3). The spin-up of stars from planet engulfment has been investigated by several studies and is expected to occur relatively frequently (Qureshi et al. 2018; Stephan et al. 2020; O'Connor et al. 2023).

We estimate Zvrk's rotational moment of inertia using the best-fitting stellar structure from our optimisation exercise in Section 3.1. To simplify our analysis further, we assume, to first order, that the whole envelope rotates with the surface rotation period of ~ 99 days, neglecting our weak constraints on radial differential rotation. Moreover, since the outer layers of such RRRGs carry most of their angular momentum — even considering their much lower density than the bulk of the star — due to their large radius, it is also safe to ignore the stellar core itself in our calculations. This yields an estimate for Zvrk's angular momentum of the form

$$J_{\rm env} = \alpha M_\star R_\star^2 \Omega, \tag{7}$$

with the moment of inertia from Zvrk's best-fitting model corresponding to $\alpha = 0.1055$. By assumption, this angular momentum would have mostly originated from the orbit of the engulfed planet,

$$L_{\rm orb} = m\sqrt{GMa(1-e^2)} \tag{8}$$

where a is the semimajor axis (SMA), and e the eccentricity, of such a planetary orbit.

In order to supply the requisite angular momentum, a companion placed in a circular orbit at Zvrk's present radius would need to be about 16 M_J, neglecting the effects of tidal dissipation entirely. This serves as an upper bound on m_p, since in reality, orbital eccentricity would permit closer periapses than semimajor axes, and in any case tidal effects at such orbital separations should drag the planet into the star long before the star could reach its current radius. Larger orbital separations, with engulfment caused by tidal dissipation and inspiral, correspond to smaller companion masses. Even following the equilibrium tide model for simplicity (e.g. Hut 1981; Eggleton & Kiseleva-Eggleton 2001), the efficiency of this tidal dissipation is rather uncertain, as the viscous dissipation timescale t_{V1} is not well-constrained for giant stars. However, candidate values for it across 3 orders of magnitude (shown in Fig. 10) all give plausible planetary masses and orbital SMAs, ranging from about 10 M_J at 0.3 au, to about 6.5 M_J at 0.67 au. These calculations all assume that the planet was very recently engulfed, at approximately its current size and evolutionary state, and that the planet's orbit had zero initial eccentricity.

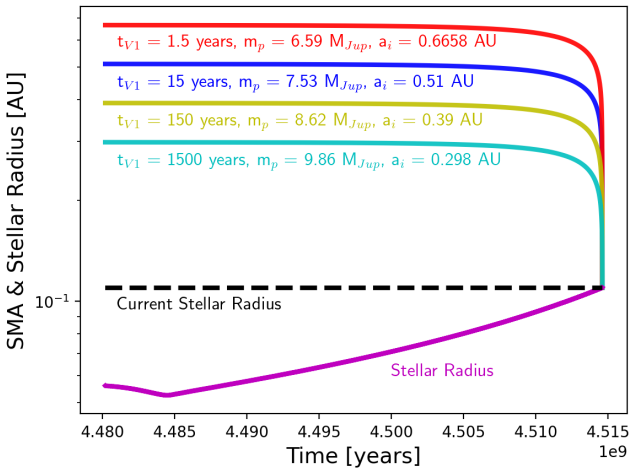

Figure 10. Tidal migration tracks of pre-engulfment planetary companions for various tidal efficiencies. The angular momentum imparted on the stellar envelope depends on the orbital semimajor axis, eccentricity, and mass of the engulfed object. Here we simulate the orbital decay and eventual engulfment of various configurations of these elements (assuming, however, circular orbits), dependent on the viscous time scale t_{V1} of the star, which is uncertain (see, for details, Appendix of Eggleton & Kiseleva-Eggleton 2001). The orbital decay is modeled such that engulfment would approximately occur at the star's current radius (shown in magenta) at its current estimated age. More efficient tidal dissipation (shown in red) would imply a planet mass of about 6.59 M_J with an initial SMA of 0.6658 au, while less efficient dissipation (shown in cyan) would imply a mass of about 9.86 M_J and an initial SMA of 0.298 au.

Another possible scenario is that the planet was originally at a much wider separation, but was able to be engulfed due to a very high orbital eccentricity (>0.9) bringing periapsis within close proximity of the star (thereby also enabling strong tidal

dissipation). Such a scenario would be possible if other bodies interacted with the system and incited high eccentricity, for example through scattering or secular processes (e.g., Weidenschilling & Marzari 1996; Chatterjee et al. 2008; Naoz et al. 2011, 2012, 2013; Stephan et al. 2018, 2021, etc.). In such a scenario the original orbit of the planet could have had an SMA of tens of au, with a minimum possible planet mass of about 6.7 M_J. This scenario, however, would require the past or current presence of additional planets or stellar companions, which are so far not detected. Nonetheless, this may warrant future investigation.

Zvrk's convective envelope is so massive (of order 10^{33} g) that no companion masses consistent with the rotational signature will be capable of producing the near-meteoritic A(Li) implied by its deep lithium absorption feature. More specifically, Zvrk would have had to ingest the lithium supply of $\sim 10^3$ gas giants to generate this chemical signature from engulfment alone. As such, this high a measured value cannot have originated purely from the engulfment or accretion of additional material. Rather, some degree of self enrichment, such as through the Cameron-Fowler process (Cameron & Fowler 1971), must also be invoked to explain it. We note that this does not preclude any engulfment or accretion from having happened historically: rather, it indicates only that lithium is a degenerate tracer of history with other formation pathways.

This need for self-pollution is difficult to reconcile with Zvrk's apparent position relative to the nitrogen enrichment sequence. A purely intrinsic origin for the observed lithium and angular momentum, with both having been brought up from the fast-rotating and nuclear-enriched core, would either require nitrogen to be somehow destroyed in the envelope, be redistributed differently from lithium, or else be incompatible with Zvrk's apparent (admittedly weakly constrained) nitrogen deficiency. Conversely, a purely extrinsic hypothesis for our derived rotational configuration, with angular momentum deposited into the envelope by either the accretion of infalling material or the engulfment of a less massive object, would produce chemical pollution compatible with the observed direction of both of these chemical anomalies, but incompatible with their observed magnitudes. Unfortunately, this tension appears only resolvable by resorting to fine-tuning some combination of scenarios (II) and (IV) — e.g., by demanding temporally separated mixing episodes for different nuclear species, as suggested in Tayar & Joyce (2022). We leave a more detailed examination of Zvrk's evolutionary history to future work.

4.2. *Magnetic Activity*

Magnetic activity in dwarfs is known to be generated by the interposition of convective turbulence with rotational shear. This can be characterised by the Rossby number $\mathrm{Ro} = P_{\mathrm{rot}}/\tau_{\mathrm{cz}}$ (e.g. Noyes et al. 1984; Brun & Browning 2017). Customarily, the convective turnover timescale τ_{cz} is evaluated in Sun-like main-sequence stellar models locally — e.g. at one pressure scale height H_p, or one mixing length, above the base of the convection zone (near the tachocline). However, since red giants are almost entirely convective by spatial extent, such a local definition is necessarily unrepresentative of Zvrk in particular. Moreover, while the base of the convection zone is colocated with the tachocline in Sun-like stars, our analysis in Section B.2 does not yield well-defined constraints on the location of Zvrk's rotational shear. As such, we evaluate the Rossby number with respect to a global convective turnover timescale instead:

$$\tau_{\mathrm{cz}} = \int_{r_1}^{r_2} \frac{\mathrm{d}r}{V_{\mathrm{conv}}}, \tag{9}$$

where $r_1 = r_{\mathrm{base}} + H_p$ and $r_2 = r_{\mathrm{top}} - H_p$, and V_{conv} is the convective velocity (which we compute from mixing-length theory). This is a similar construction to that also used for fully convective dwarfs, which likewise do not possess a well-defined tachocline. Evaluating this quantity with respect to the best-fitting model in our optimisation exercise in Section 3.1, in conjunction with our nominal photometric rotational period, gives us $\mathrm{Ro}_\star \sim 0.28$. By contrast, computing this quantity from a solar-calibrated MESA model with the same physics yields $\mathrm{Ro}_\odot = 1.38$. Roughly speaking, lower values of the Rossby number indicate greater magnetic activity. The convective turnover timescale that we have obtained, ~ 350 days, is comparable to the timescales over which the amplitude of the photometric variability presented in Section 2.2 appears to evolve, and so we cannot rule out a convective origin for the surface features producing this signal. However, our subsolar model value of the Rossby number generated using this same timescale also indicates that Zvrk is possibly magnetically active, which is consistent with an interpretation of this variability as being that of surface magnetic features, potentially spots, rotating into and out of view on the visible disk.

Aside from spotting, any putative surface magnetism is known to express itself on active dwarfs in the time domain, in the form of flares and eruptive outbursts. Were it to be magnetically active, it is possible that Zvrk also participates in such transient events. We identify at least one possible marginal detection of a flare in Zvrk's PDCSAP lightcurve (shown in Fig. 11 at BTJD 2250.7, along with samples from the posterior distribution of fits to it of an impulse-exponential-decay model). Should flares actually occur on Zvrk, we should also expect to see occasional outbursts of energetic photons. Indeed, we find that near-UV photons have historically been detected from Zvrk's sky position in archival GALEX data (Million et al. 2016). We defer a more detailed investigation of this possible magnetic activity to a future work.

4.3. *Rotational Age Constraints*

While rapid for a red giant, Zvrk's surface rotation remains far slower than its breakup rotation rate, $\Omega_{\mathrm{crit}} = \sqrt{GM/R^3}$. From our seismic constraints on Zvrk's mass and radius, we find $P_{\mathrm{crit}} = 2\pi/\Omega_{\mathrm{crit}} \sim 12.5$ d: far more rapid than the observed surface rotation rate. Admittedly, both Zvrk's rotational period and this breakup rotation rate would have changed significantly over the course of its evolution up the red giant branch. To examine this, we show retrodictions for Zvrk's surface and

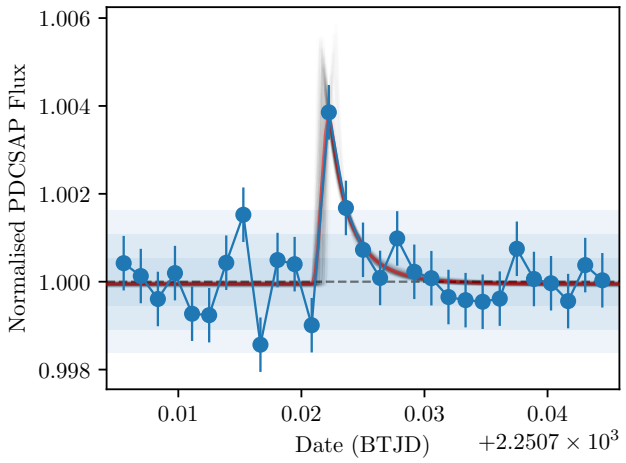

Figure 11. Candidate flare identified in two-minute-cadence PDCSAP data, scaled by the mean value, so that the data points shown here are normalised to 1 (marked with the horizontal line). The horizontal bars show integer multiples of the baseline photometric scatter of data points in the 1.5 hours immediately following the peak identified here. The faint gray lines show draws from the posterior distribution over an impulse-exponential-decay model, as fitted to the main peak using nested sampling. The median of the light-curve models from the posterior distribution is shown with the thick red line.

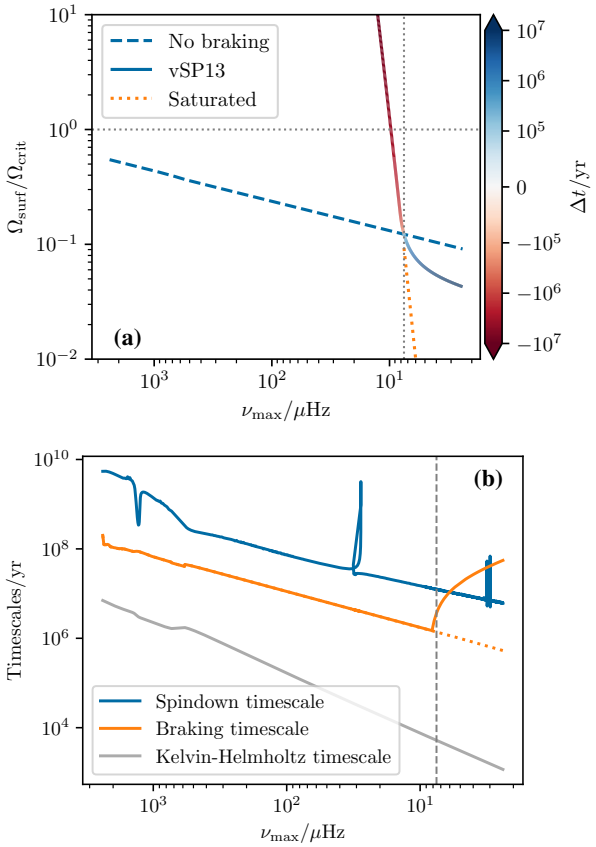

Figure 12. Rotational evolution of Zvrk under different extremal scenarios. **(a)** Evolution of the surface rotational frequency $\Omega_{\rm surf}$ from the main sequence up the RGB, using the frequency of maximum power $\nu_{\rm max}$ as an evolutionary proxy, and shown as a fraction of the breakup rotational frequency $\Omega_{\rm crit}$ (horizontal dotted line). The solid curve shows magnetic braking according to the prescription of van Saders & Pinsonneault (2013), where line segments are coloured by simulation time Δt from the present (i.e. positive represent integration into the future). The dotted curve shows rotational evolution from the present under braking parameters chosen to produce unsaturated braking, while the dashed curve shows the most permissive scenario of no magnetic braking (i.e. angular momentum is conserved). The vertical dotted line indicates $\nu_{\rm max}$ of our best-fitting model. **(b)** Comparison of several characteristic timescales. We show in particular the spindown timescale $|P_{\rm rot}/\dot{P}_{\rm rot}|$ associated with structural expansion in the absence of magnetic braking; the braking timescale $|J_{\rm tot}/\dot{J}_{\rm tot}|$ associated with angular momentum loss by the prescription of van Saders & Pinsonneault (2013), with the dotted curve showing the same saturated trajectory as in panel (a); and the Kelvin-Helmholtz timescale $t_{\rm KH} = GM^2/2RL$, as a proxy for the thermal readjustment timescale.

breakup rotation rates in Fig. 12a, generated by integrating backwards from the present day — at which we impose a notional rotational period of 100 d, indicated with the vertical line — along the best-fitting evolutionary track from our optimisation exercise in Section 3.1. We plot in particular the surface rotation rate as a fraction of the breakup rotation rate, showing with the dashed curve a counterfactual scenario with no magnetic braking. Under this extremely permissive scenario, Zvrk would have been rotating at half its breakup rotation rate on the main sequence.

However, if we are to interpret the apparent photometric variability as spot modulations, the same magnetic field that drives this spot activity, and the possible flaring that we discuss above, ought also to be responsible for magnetic rotational braking. Such a high rotation rate would, in an actual star, almost surely be braked. In turn, the action of any magnetic braking whatsoever would require Zvrk to initially have been rotating still faster, in order to match its present observed rotational period on the red giant branch. While the breakup rotation rate $\Omega_{\rm crit}$ should also have been faster at earlier times, its evolution is driven by structural expansion, which operates on far longer timescales than magnetic braking. To illustrate this, we show with the solid curve in Fig. 12a a retrodiction generated using the magnetic braking prescription of van Saders & Pinsonneault (2013), with an angular momentum loss rate of

$$\dot{J} \propto f_K \Omega^3 \min\left(1, \frac{\omega_{\rm crit}\tau_{\rm cz,\odot}}{\Omega\tau_{\rm cz}}\right)^2. \qquad (10)$$

This can be seen to scale either as $\dot{J} \propto \Omega$ for rotation rates above an inverse-Rossby-number saturation threshhold, $\Omega\tau_{\rm cz} > \omega_{\rm crit}\tau_{\rm cz,\odot}$ (the "saturated regime"), or to give $\dot{J} \propto \Omega^3$ for lower rotation rates (the "unsaturated regime"). For this exercise, we adopt a standard value for the saturation rota-

tion rate of $\omega_{\rm crit} \sim 12\Omega_\odot$, and a normalisation constant for the angular momentum loss rate of $f_K = 9.37$, calibrated to produce the solar equatorial rotation rate of 25.4 d for our solar-calibrated MESA model with a disk rotation period of 8 d and a disk-locking timescale of 1 Myr. This setup is generally in keeping with previous uses of this angular-momentum-loss prescription. The initial conditions of our integration are again chosen to produce a rotational period of 100 d at the present observed value of $\nu_{\rm max}$. We colour this solid curve according to simulation time $\Delta t = t - t_{\rm present}$.

Fortuitously, our chosen combination of solar-calibrated f_K, $\omega_{\rm crit}$, and $\tau_{\rm cz}$ are such that Zvrk leaves the saturated regime very shortly before the present day in our retrodictions. Zvrk otherwise experiences saturated braking ($\dot{J} \propto \Omega$) in most of its preceding evolution up the RGB. Under this scenario, Ω increases very rapidly with lookback time. In order to produce its present rotation rate in the presence of magnetic braking, Zvrk must have been rotating at or faster than the breakup rotation rate $\Omega_{\rm crit}$ within about 5 Mya, when it was already a quite evolved red giant ($\nu_{\rm max} < 20\,\mu$Hz). This is incompatible with Zvrk's angular momentum having been of primordial origin, ruling out a single-star hypothesis (scenario (I) in Section 4.1) for Zvrk's rotational configuration. Were Zvrk's rotation to have resulted from an engulfment, this also ought to have happened less than 5 Mya, as only later engulfments could have deposited enough angular momentum to both match Zvrk's present rotation rate after braking, and yet also not exceed its breakup rotation rate at the time of engulfment.

This same magnetic braking would also place an upper limit on how long we would expect such a rotational signal to persist after the event. We show a comparison of the timescales in Fig. 12b. The spindown timescale owing to structural expansion in the absence of magnetic braking, $|P_{\rm rot}/\dot{P}_{\rm rot}|$, shown with the blue curve, can be seen to be much slower than the magnetic braking timescale $|J_{\rm tot}/\dot{J}_{\rm tot}|$, shown in orange. For the latter, the solid curve shows the scenario depicted in Fig. 12a, where Zvrk's magnetic braking leaves the saturated regime shortly before the present day. We also consider a more aggressive braking scenario, where we extrapolate from its present rotational configuration under the assumption that the magnetic braking remains saturated, shown with the dotted curves on both Fig. 12a and b. However, even this more pessimistic scenario can still be seen to yield braking (and so rotational persistence) timescales far longer than the Kelvin-Helmholtz timescale, shown in gray, which we use as a proxy for the thermal readjustment timescale. This is significant because any engulfment hypothesis for the deposition of angular momentum into a red giant's envelope would also necessitate heating the envelope, causing the red giant to puff up in response, and resulting in anomalously cool observed temperatures (as predicted in O'Connor et al. 2023 and Yarza et al. 2023, and reported in Patton et al. 2023). Since thermal readjustment can be seen to occur over much shorter timescales than even aggressive, saturated, rotational braking, our observational determination of Zvrk as being both rapidly rotating, and yet not too spectroscopically unusual, appears compatible with an engulfment hypothesis.

5. CONCLUSION

We have determined that TIC 350842552, or "Zvrk" for short, is a rapidly-rotating first-ascent red giant. We have measured Zvrk's rotation rate with independent uses of asteroseismology, photometry (from space and from the ground), and spectroscopy (from rotational Doppler broadening). Our constraints on Zvrk's global properties and structure, derived from detailed asteroseismic modelling against constraints from individual mode frequencies, suggest that all of these rotational measurements are mutually consistent with each other. We have further developed, and then employed, new techniques in asteroseismic rotational analysis — making use of recent theoretical developments permitting pure p-modes to be disentangled from the usual spectrum of mixed modes — to constrain properties of Zvrk's radial differential rotation independently of the radiative core. Together, these paint a picture of Zvrk as being differentially rotating in its envelope, and possessing rotational shear in the sense of the rotation rate increasing outwards at some point: a similar configuration to that proposed for a far less evolved red giant in Tayar et al. (2022).

Aside from this anomalous rotation, we have additionally found Zvrk's envelope to be simultaneously almost meteoritic in its lithium enrichment, and also potentially less enriched in ^{14}N than typical for its mass, suggestive of recent pollution. Zvrk's high surface rotation rate, combined with astrophysical constraints from magnetic braking, suggests an engulfment event as both a source of this angular momentum, and a trigger for any self-enrichment. We place limits on how long ago such an engulfment could have occurred — no more than several million years ago. With such a recent engulfment, Zvrk's angular momentum content suggests a mass for the engulfed object of roughly 7 to 9 M_J, orbiting a little closer in than 1 au. These orbital parameters are fairly consistent with existing demographic studies of giant planets (e.g. Kennedy & Kenyon 2008; Wittenmyer et al. 2020). However, a more detailed examination of both this engulfment, and any self-enrichment episode that it may trigger, will be necessary to reconcile Zvrk's multiple chemical anomalies. This we leave to future work.

Our characterisation of Zvrk demonstrates the diagnostic power of asteroseismology as a tool for not merely measuring rotation rates in field stars, but indeed for initially detecting rotation in the first place. The asteroseismic rotational signature remained robust against aggressive preprocessing, which had rendered direct measurement of quasiperiodic variability from the same data set otherwise nonviable. Moreover, in order to relate Zvrk's observed seismic rotational signatures to its interior structure, we have had to devise new asteroseismic techniques altogether. These new tools might also be applied to other known lithium-anomalous post-main-sequence stars, many of whose rotational properties are currently even more poorly constrained. It is also not yet well understood how

efficiently such massive objects as we propose to have been engulfed would be disassociated were they actually to be deposited into a red giant envelope (e.g. Jia & Spruit 2018; Yarza et al. 2023). While our poor constraints on the structure of Zvrk's rotational shear yield no insight on this, we anticipate firmer constraints on envelope rotational shear, which would naturally emerge with higher-quality data and/or longer time series, to better illuminate such disruption. More generally, a better understanding of such engulfment events may help to explain the origins of the current, known, population of isolated RRRGs with no detectable companions. Some of these RRRGs are also known to be magnetically active (e.g. Gehan et al. 2022), and the potential links between this magnetic activity and post-main-sequence rotation may also be worth further investigation. Additionally, in the high-eccentricity engulfment scenario that we have considered, the planet's original orbit would potentially have been strongly misaligned with the pre-engulfment stellar rotational axis, which would result in rotational misalignment between Zvrk's core and envelope upon engulfment. While seismic diagnostics of any such possible misalignment would be valuable in disambiguating between engulfment scenarios, existing methods do not yet permit us to place constraints of this kind.

Over broader horizons, Zvrk also serves as a demonstration of both the limitations of the presently available TESS data, and the pressing need for sustained and consistent investment in long time series for asteroseismic purposes. Between our initial asteroseismic detection and the writing of this paper, a few extra months of a third year of TESS CVZ coverage, in Cycle 5, have been collected. We have found the addition of a few months not to provide any noticeable improvements to any of our asteroseismic constraints. However, given the proposed longevity of the TESS mission (potentially decades as advertised), long-term monitoring might yield qualitative improvements in our asteroseismic constraints. Supplemental monitoring from future space missions (e.g. PLATO) will also relieve TESS of our demands on its duty cycle. In addition to permitting multiplet splittings to be constrained without pooling as we have done, decades-long monitoring will also be a bare minimum requirement for any prospect of, e.g., measuring core rotation rates from stars as evolved as Zvrk. Were they available, these measurements would bound their total angular momentum content, instead the present situation of the core being an invisible angular momentum sink. This would in turn greatly constrain their possible histories.

Finally, as for Zvrk itself, much remains about it to be observationally determined. Should it actually be flaring, Zvrk would make a compelling target for future space-based UV photometry missions. Moreover, although Zvrk's Gaia RUWE and RV scatter are not consistent with a binary companion with orbital periods close to the Gaia baseline, it cannot definitively rule out the presence of a very widely separated orbital companion, which may have caused a high-eccentricity engulfment scenario (e.g. Knutson et al. 2014), or any potential undetected close-in companions undergoing tidal decay. Zvrk's southerly location renders it amenable to contemporaneous follow-up radial-velocity observations for this purpose using cutting-edge instruments, such as ESPRESSO (for now) and G-CLEF (in the near future). Other kinds of follow-up observations, such as speckle imaging, may also prove fruitful. All of these paths lead far beyond the scope of this paper, but there is clearly much more work to be done.

We thank S. Basu, T. Bedding, and S. Hekker for constructive feedback on preliminary versions of this work, and C. Hayes, J. Hinkle, and A. Boesgaard for productive discussions. MTYH and MSF thank the Aspen Center for Physics for their hospitality during the completion of parts of this work. The Jupyter notebooks and MESA inlist files used for this work, and the source of this paper itself, can be found on a GitHub repository at http://github.com/darthoctopus/zvrk; the repository will be made public upon acceptance.

This paper includes data collected by the TESS mission. Funding for the TESS mission is provided by the NASA's Science Mission Directorate.

This work has made use of data from the European Space Agency (ESA) mission *Gaia* (https://www.cosmos.esa.int/gaia), processed by the *Gaia* Data Processing and Analysis Consortium (DPAC, https://www.cosmos.esa.int/web/gaia/dpac/consortium). Funding for the DPAC has been provided by national institutions, in particular the institutions participating in the *Gaia* Multilateral Agreement.

JMJO, MTYH, and MSF acknowledge support from NASA through the NASA Hubble Fellowship grants HST-HF2-51517.001-A, HST-HF2-51459.001-A, and HST-HF2-51493.001-A, respectively, awarded by STScI. STScI is operated by the Association of Universities for Research in Astronomy, Incorporated, under NASA contract NAS5-26555. APS acknowledges partial support by the Thomas Jefferson Chair Endowment for Discovery and Space Exploration, and partial support through the Ohio Eminent Scholar Endowment. MY, ZÇO, and SÖ acknowledge the Scientific and Technological Research Council of Turkey (TÜBİTAK:118F352).

Software: NumPy (Harris et al. 2020), SciPy stack (Virtanen et al. 2020), AstroPy (Astropy Collaboration et al. 2013, 2018), `Comove` (Kraus & Rizzuto 2022), `dynesty` (Koposov et al. 2022), Pandas (Reback et al. 2021), MESA (Paxton et al. 2011, 2013, 2015, 2018, 2019), GYRE (Townsend & Teitler 2013), `ADIPLS` (Christensen-Dalsgaard 2008)

Facilities: TESS, ASAS-SN, APOGEE, GALAH, WISE, GALEX

APPENDIX

A. RESULTS OF PEAKBAGGING PROCEDURE

We illustrate the posterior distributions arising from our nested-sampling procedure in Fig. A1. These joint distributions include both the shared properties describing the power spectrum as a whole, and all of the modes collectively (main figure), as well as the properties of each individual multiplet (inset). For the purposes of stellar modelling, we assume that all rotational splittings are symmetric (i.e. no perturbations to the mode frequencies arising from latitudinal differential rotation or magnetic fields), and use the notional $m = 0$ mode frequencies associated with our parametric model, Eq. (2), as constraints on the $m = 0$ mode frequencies returned from MESA stellar models. We provide our fitted values of these mode frequencies in Table A1. For each mode, we report a posterior median and the size of the 1-σ credible region around this median, computed from the marginal posterior distribution for its nonrotating frequency. We also provide our identification of the degree ℓ, and of the p-mode radial order n_p, supplied through the asymptotic relation, Eq. (1).

Table A1. Notional $m = 0$ p-mode frequencies from peakbagging procedure with multiplet model

ℓ	ν/μHz	e_ν/μHz	n_p
0	5.81	0.01	4
0	6.91	0.02	5
0	8.20	0.02	6
0	9.41	0.05	7
0	10.66	0.03	8
1	5.34	0.03	3
1	6.40	0.01	4
1	7.64	0.01	5
1	8.78	0.02	6
1	10.09	0.03	7
2	5.63	0.05	3
2	6.70	0.02	4
2	7.90	0.03	5
2	9.17	0.02	6
2	10.43	0.04	7

B. GENERALISED ROTATIONAL INVERSIONS

In principle, each observed rotational multiplet permits us to probe Zvrk's internal rotational profile $\Omega(r)$ with sensitivity to different parts of the stellar interior. In the perturbative regime of slow rotation, where $\Omega \ll 2\pi\Delta\nu$, the spacing between modes in a rotational multiplet is related to $\Omega(r)$ through an integral expression of the form (e.g. Gough 1981; Gough & Thompson 1990)

$$\omega_{n\ell m} - \omega_{n\ell 0} \equiv m\,\delta\omega_{n\ell} \sim m\beta_{n\ell}\int K_{n\ell}(r)\Omega(r)\mathrm{d}r, \qquad \text{(B1)}$$

where β is an overall sensitivity constant, and K is a normalised integral kernel, associated with a mode indexed by n and ℓ. For low-degree p-modes, $\beta \to 1$ in the limit of large n_p and/or large ℓ, while for g modes, $\beta \to 1 - 1/\ell(\ell+1)$ in the same limit. If a large enough number of rotational multiplet splittings $\delta\omega_{n\ell}$ have been measured precisely, Eq. (B1) may be inverted to yield inferences about the nature of the rotational profile. There are two main classes of methods by which such "rotational inversions" have been performed in the asteroseismic literature, both inheriting in large part from similar efforts in helioseismology (e.g. Schunker et al. 2016a,b; Eggenberger et al. 2019a). In the method of optimally localised averages (OLA: e.g. Backus & Gilbert 1968), one chooses judiciously some linear combination of $\beta_i K_i$ such that the coadded kernels approximate an averaging kernel of finite width localised at some preselected position r_0, with the shape of this kernel, and the quality of this approximation, being determined by some optimal compromise between spatial resolution and effective measurement uncertainty (e.g. MOLA: Gough 1985; SOLA: Pijpers & Thompson 1994); that same linear combination of $\delta\omega_i$ then approximates $\Omega(r_0)$. A full picture of $\Omega(r)$ is built up by repeating this procedure for various choices of r_0. By contrast, in the regularised least-squares (RLS) method (e.g. Christensen-Dalsgaard et al. 1990), one first parameterises a subset of permissible rotational profiles, and then uses Eq. (B1) to generate predictions for the multiplet rotational splittings; an optimal description of the rotational profile from this subset is then found by minimising the discrepancy between the predicted and measured rotational splittings, in a least-squares sense, with the potential inclusion of additional regularisation to penalise e.g. discontinuities and other pathological features.

Rotational inversions in evolved stars have mostly been applied to dipole modes of mixed gravitoacoustic character. Morphologically, the rotational kernels of these mixed modes are combinations of g-mode components, which abruptly truncate at the radiative core boundary, and p-mode components, which sample the envelope and are insensitive to the radiative core. Such a combination has historically been described with a mixing fraction ζ in the form $\beta_{\mathrm{mixed},n\ell}K_{\mathrm{mixed},n\ell} = \zeta\beta_{\mathrm{g},n\ell}K_{\mathrm{g},n\ell} + (1-\zeta)\beta_{\mathrm{p},n\ell}K_{\mathrm{p},n\ell}$ (Goupil et al. 2013). However, since ζ is determined by the proximity of mixed modes to the underlying p- and g-modes as they undergo avoided crossings, small changes to the frequencies of these underlying modes may result in large changes to ζ — particularly where the coupling strength between the mode cavities is weak — for the most p-dominated mixed modes which are closest to these avoided crossings, and which are most amenable to observation. Equivalently, the radius of convergence for perturbative expansions for the rotating mode frequencies, of which linear expressions like Eq. (B1) are but the first-order term, is significantly reduced for near-degeneracy configurations like those seen in red giants (Deheuvels et al. 2017; Ong et al. 2022). Any use of these mixed-mode kernels to perform inversions (not merely rotational) would accordingly be highly sensitive to small differences in the structure — and thus, on the red

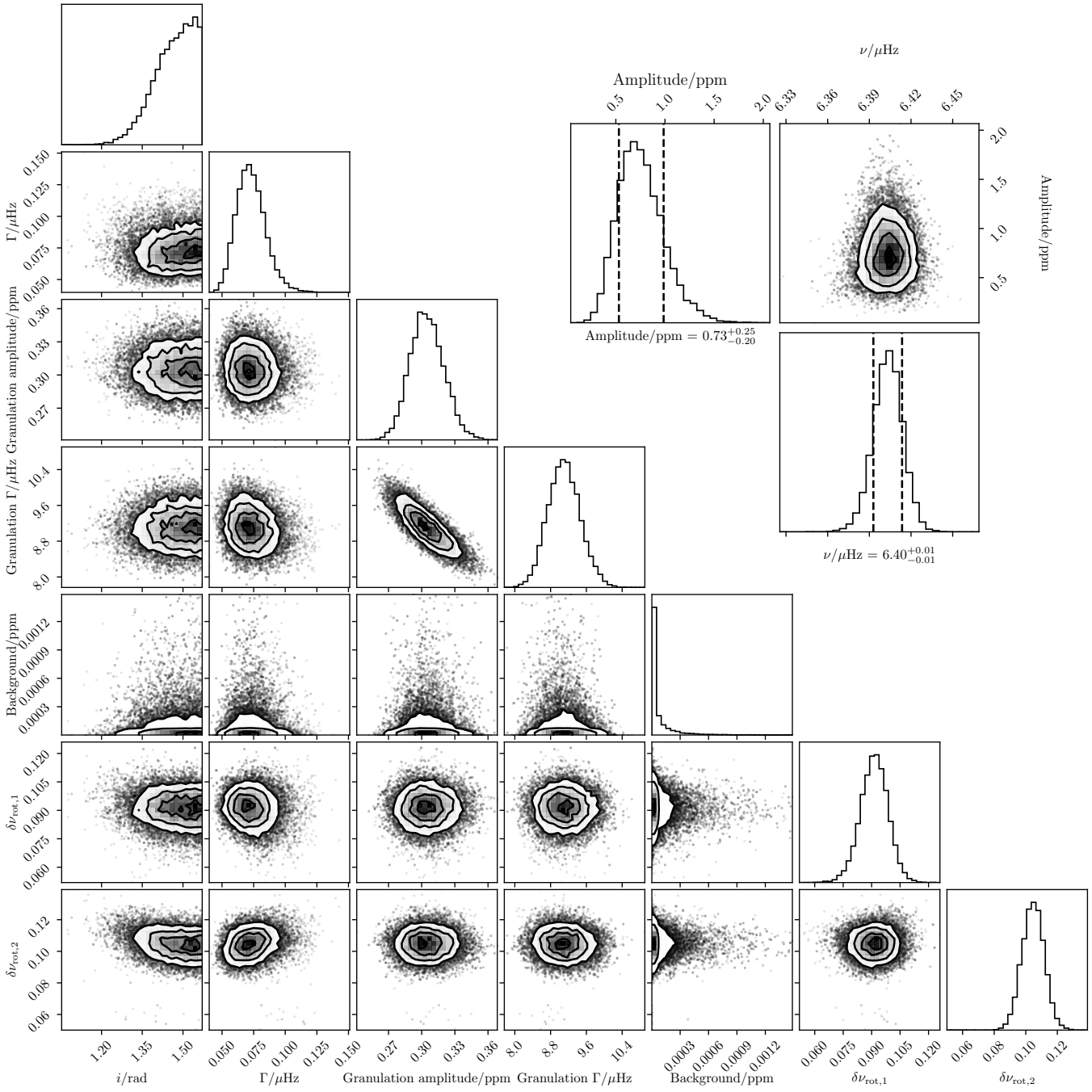

Figure A1. Posterior distributions for quantities returned from nested-sampling peakbagging procedure. The main figure, in the lower left, shows the joint posterior distribution for quantities entering into Eq. (2) that are pooled between modes. In particular, we see that there is mild correlation between some properties of our background model (labeled "Granulation" here), but the quantities of asteroseismic relevance are constrained to be statistically independent of each other, aside from a very mild correlation between the axial inclinations i, the pooled linewidths Γ, and the rotational splittings $\delta\nu_{\mathrm{rot},\ell}$. The dipole-mode rotational splitting can be seen to be smaller than that of the quadrupole modes. The inset figure, shown in the upper right, shows the joint distribution for quantities associated with the dipole mode closest to ν_{max} (i.e. $n_p = 5, \ell = 1$), where again the notional nonrotating frequency ν is constrained independently from the mode amplitude. The joint distribution between modes also indicates that the mode frequencies for all modes are independent of each other (although that corner plot is too large to fit on a single page). The mode frequencies derived from nested sampling in this fashion, and their uncertainties, are reported in Table A1.

giant branch, evolution — of the reference models used to generate these kernels numerically, compared to that of the actual star. Obversely, the stellar structure would have to be constrained exquisitely well, both precisely and accurately, in order for inversions to be feasible with mixed modes.

For these reasons, rotational inversions have never been attempted on red giants as evolved as Zvrk, since the coupling between its p- and g-mode cavities is exceedingly weak, which, ordinarily, would render its mixed-mode kernels pathologically sensitive to ζ. However, since this coupling is so weak as to be observationally irrelevant, we now apply new techniques to generate notional pure p-mode kernels, and perform inversions with respect to them instead. Since per-multiplet rotational splittings are not available, we also generalise existing rotational-inversions techniques to operate with respect to the power spectrum directly, rather than with respect to preprocessed mode frequencies.

B.1. *Rotational Kernels*

Having isolated Zvrk's p-mode cavity through the π-mode construction of Ong & Basu (2020) in our fitting and optimisation exercises, we now compute its rotational kernels using π-mode eigenfunctions, as described in Ong et al. (2022). In order for such pure p-mode kernels to be used in inversion problems for subgiants and less evolved red giants, the notional "pure" p-mode rotational splittings must be determined from a set of mixed modes. In general, this remains an open problem. Fortunately, the observational irrelevance of any coupling to the g-mode cavity works in our favour here, as we already have effectively measured the p-mode rotational splittings directly, rendering the problem moot.

Freed of any dependence on the g-mode cavity, the pure p-mode rotational kernels turn out to be extremely robust to even large variations in structure and evolution. We show in Fig. B1 how they evolve over a very large range of $\nu_{\max}$ — from double to half of our nominal observed value — over the course of the best-fitting evolutionary track from our optimisation exercise. Specifically, we show in Fig. B1a the evolution of a representative rotational kernel — that associated with the $n_p = 6, \ell = 1$ mode — plotted as a function of fractional radius. The overall morphology and normalisation of this kernel, as well as the locations of null sensitivity, can be seen to remain extremely stable despite the very large range of $\nu_{\max}$ considered here. This is as opposed to the behaviour of mixed-mode kernels, where relative fractional sensitivity to the core, which is determined by ζ, would vary rapidly over time, as p-modes evolve onto and off resonance with the underlying g-modes. Likewise, the overall normalisations β are also very stable (Fig. B1b), changing by no more than 1% over a large range of $\nu_{\max}$. Again, this is stark contrast with mixed modes, whose overall normalisations $\beta \sim \zeta\beta_g + (1-\zeta)\beta_p$ would switch between 1 and $1 - 1/\ell(\ell+1)$ as modes evolve through avoided crossings. Thus, despite the TESS data having constrained Zvrk's structure in Section 3.1 with somewhat less precision than has traditionally been possible with *Kepler*, we can be reasonably confident that our subsequent attempts at inspecting its rotational stratification using p-mode kernels will remain robust against potential systematic misestimates of its interior structure, unlike the conventional situation with mixed-mode kernels.

The morphology of the kernel shown in Fig. B1a is typical of the pure p-mode rotational kernels encountered in helioseismology, and in the asteroseismology of main-sequence stars. Its sensitivity can be seen to be concentrated towards the surface, as are its zero points. Thus, if we were to place uninformative priors on the localisation of rotational shear, such priors cannot be uniform in the physical radial coordinate, but must rather be proportional to the apparent envelope, and density of zeros, of these kernels. To ease our subsequent analysis, we will find it beneficial to reparameterise these kernels into a radial coordinate system such that uninformative priors are also uniform in our preferred radial coordinate. For this purpose, we choose to use the acoustic radius, $t(r) = \int_0^r (1/c_s)\mathrm{d}r$, as our preferred radial coordinate (as originally proposed in Pijpers & Thompson 1994). The p-mode displacement eigenfunctions are known to admit an approximate description in terms of Riccati-Bessel functions of the first kind[2], s_ℓ (see e.g. Roxburgh 2010; Lindsay et al. 2023):

$$\psi_r \equiv r\sqrt{\rho c_s}\xi_r \sim s_\ell(\omega t + \delta_\ell), \tag{B2}$$

where c_s is the sound speed, and δ_ℓ is an inner phase function with only weak dependence on frequency and position away from $t = 0$ and $t = T$. Since the p-mode eigenfunctions are orthogonal with respect to the integral measure $r^2\rho$ when integrated with respect to the physical radial coordinate, the scaled wavefunctions ψ form an orthogonal basis with respect to the unit measure when integrated with respect to the acoustic radial coordinate. Thus, we may treat a uniform prior on the acoustic radius as being uninformative. Under the action of such reparameterisation, the kernels themselves transform as $K_t(t) = c_s K_r(r(t))$. We show the $n_p = 6, \ell = 1$ kernel under the action of this reparameterisation in Fig. B1c, plotting the kernels now as functions of the fractional acoustic radius. Again, we see that any variations to the shape and the loci of sensitivity arising from structural evolution are slight. Away from the boundaries set by the centre and the surface of the star, the shape of the kernels is roughly sinusoidal; this is because the Riccati-Bessel functions appearing in Eq. (B2) may be approximated as sinusoids at large argument (Arfken & Weber 2005), so this is a property of p-modes generally, and not just this mode in particular. For illustration, we also show a similar diagram for the $n_p = 6, \ell = 2$ p-mode in Fig. B1d, which exhibits much the same qualitative insensitivity to evolution.

A further consequence of our use of pure p-mode rotational kernels is that, as can be seen in Fig. B1, the nonradial p-

[2] These are related to the usual spherical Bessel functions of the first kind as $s_\ell(x) = x j_\ell(x)$. Here we use lowercase s rather than the more conventional uppercase to avoid confusion with the Lamb frequency, which is also written as S_ℓ in the context of asteroseismology.

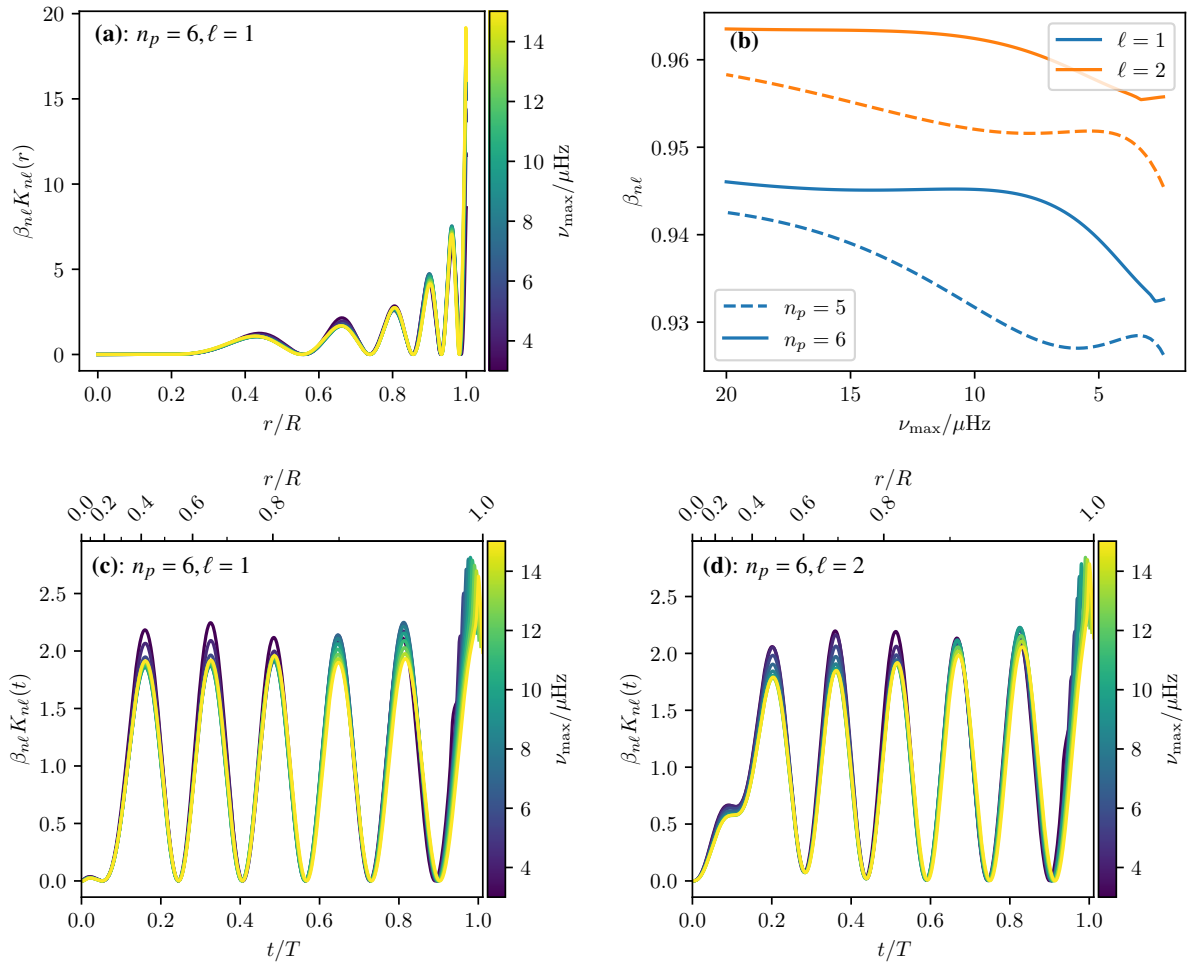

Figure B1. Stability of pure p-mode rotational kernels to stellar evolution. **(a)** Rotational kernel of the $n = 6, \ell = 1$ p-mode, shown as a function of fractional physical radius for $\nu_{\max}$ between half and double the observed value. Despite the large range of $\nu_{\max}$ considered, the shape of the kernel can be seen to remain very stable, unlike those of mixed modes. **(b)** Variations in the overall sensitivity β of several p-mode kernels over the course of evolution (using $\nu_{\max}$ as its proxy). Rather than rapidly switching between 1 and $1 - 1/\ell(\ell+1)$ as those of mixed modes would, the sensitivity of p-mode kernels remains very stable over time. **(c)** The same kernel as (a), but reparamaterised to permit the use of the acoustic radius t rather than the physical radius r as the integration variable. **(d)** The same transformation applied to the $n_p = 6, \ell = 2$ kernel. The shape of the kernel (particularly close to the centre of the star) can be seen to be slightly different. It can also be seen to be likewise insensitive to evolution.

mode wavefunctions decay to zero at small radius, and so these kernels are almost entirely insensitive to the radiative core (whose boundary is situated in our best-fitting stellar structure at $r/R \sim 0.03$). For rotational inferences made using mixed modes, it is common to parameterise radial differential rotation in terms of a phenomenological two-zone model, with the core and envelope treated as separately rotating solid bodies (e.g. Klion & Quataert 2017; Triana et al. 2017; Mosser et al. 2018; Gehan et al. 2018; Eggenberger et al. 2019b; Fellay et al. 2021; Ahlborn et al. 2022). By contrast, any constraints on radial differential rotation that we might obtain using our observed p-modes, through these p-mode rotational kernels, will be localised entirely within the convective envelope.

B.2. *Radial Differential Rotation*

Our marginal posterior distribution for the difference between the dipole and quadrupole rotational splittings, Fig. 3, suggests that Zvrk's envelope is not rotating as a solid body, and possibly exhibits radial differential rotation. Given the preceding discussion, we might wish to investigate this differential rotation using existing rotational inversion techniques. However, our attempts to do so are hindered by the limitations of the existing TESS data set — including its poorer photometric stability, redder bandpass, and presently shorter duration compared to the nominal *Kepler* mission — which resulted in us having to pool measurements of the rotational splitting width between different modes in Section 2.1. Even then, each of our pooled rotational splittings is constrained with less precision than that of individual multiplets in *Kepler* data (e.g. as in Tayar et al. 2022). Were we to have constrained

these splittings for each multiplet individually, the resulting uncertainties would be larger still — too large for the rotational inversion techniques that we have described above to be feasibly prosecuted. To proceed further, we must adapt existing methods to this present situation where we have only indirect access to the individual multiplet splittings, $\delta\omega_{n\ell}$.

We first consider how the OLA method may be adapted to operate with respect to our pooled rotational measurements. We observe that the pooled rotational splitting for dipole modes must be related to those of the underlying individual dipole multiplets through some kind of visibility-weighted averaging procedure, not necessarily linear. If we approximate this with a linear combination of mode-wise rotational splittings as $\delta\omega_{\ell=1} \sim \sum_{n,\ell=1} w_n \delta\omega_{n,\ell}$, then the corresponding linear combination of dipole-mode kernels effectively provides us with a "pooled" sensitivity kernel, $K_{\mathrm{eff},1}$, for the observed dipole rotational splitting. We may also divide the averaged splitting by the associated linear combination of sensitivity constants, $\langle\beta_1\rangle = \sum_{n,\ell=1} w_n \beta_{n\ell}$, to yield an estimate of $\Omega(t_1)$ as localised by this pooled kernel. Such an estimate is localised, roughly speaking, at the centre of sensitivity for this pooled kernel, $t_1 = \int t \cdot K_{\mathrm{eff},1}(t)\,\mathrm{d}t$. Since we have two averaged rotational splittings at our disposal — one for dipole modes, and one for quadrupole modes — we in principle then should be able to constrain rotational shear in terms of the differences in localised rotation rates, $\Delta\Omega \sim \Omega(t_2) - \Omega(t_1)$, as well as differences in the locations at which these estimates are made, $\Delta t = t_2 - t_1$.

It remains for us to determine how these coefficients w_i are to be related to the mode visibilities. By ansatz, we set $w_i \propto H_i$, the observed mode heights appearing in Eq. (2). Through the above discussion, we may then evaluate $\Delta\Omega$, Δt, and the per-degree pooled kernels in closed form, given values for all of the nonradial mode heights and averaged rotational splittings. Since our nested-sampling procedure in Section 2.1 provides us with a large number of samples from the joint distributions between all of these quantities, applying this procedure to all of these samples permits us to estimate the entire posterior distributions for $\Delta\Omega$, Δt, and the pooled kernels themselves, constrained directly by the power spectrum.

We examine these posterior distributions in Fig. B2. In Fig. B2a, we show the marginal distributions for $\Delta\Omega$ (top) and Δt (bottom), in both cases marking out 0 with a dashed line, which is the value demanded by a null hypothesis of solid-body rotation. We find that $p(\Delta\Omega > 0) \gtrsim 0.85$, weakly suggesting that rotational shear is indeed present, although unfortunately we are not able to rule out the null hypothesis altogether. Since we have defined Δt in the sense $t_2 - t_1$, rudimentary JWKB analysis would suggest that it be positive, as the inner turning points of the quadrupole p-modes, set by where the Lamb frequency $S_\ell = \sqrt{\ell(\ell+1)}c_s/r$ matches the mode frequency ω, lies outside of that of the dipole modes. Contrary to this expectation, the posterior distribution for Δt is more consistent instead with negative values. This would indicate that the inner portions of the convective envelope are rotating more quickly than the outer portions.

We examine these kernels in more detail in Fig. B2b, where we plot with the faint thin curves 100 samples from the posterior distribution over both pooled kernels, and with the thick solid curves the posterior median pooled kernels, using different colours for each degree. Additionally, we mark out the location of the JWKB inner turning points (evaluated at $\nu_{\max}$) from our best-fitting model with vertical dashed lines, in matching colours. The quadrupole inner turning point can indeed be seen to lie exterior to the dipole inner turning point. However, the shape of the quadrupole-mode pooled kernel can also be seen to be more spread out than the dipole-mode kernel. Ultimately, this is because the expressions for the rotational kernels contain explicit dependence on ℓ through contributions from a term $[\ell(\ell+1)-1]\xi_h^2$, in addition to the implicit dependences of the eigenfunctions themselves on ℓ. For low-degree p-modes, the displacement eigenfunctions become approximately radial in the outer parts of the star, where the approximation of plane-parallel stratification holds well. Thus, this degree-dependent enhancement to the rotational kernel from the horizontal component of the eigenfunction is most significant near the interior of the star. Accordingly, the quadrupole-mode kernels feature a "leg" protruding inwards from their first local maximum after the inner turning point, which is not present in the dipole-mode kernels. This has the effect of rendering the quadrupole-mode kernels more spread out compared to the dipole mode kernels, and of moving their centres of sensitivity inwards (shown with the dotted vertical lines). For Zvrk in particular, this adjustment to the centre of sensitivity is comparable to, and slightly larger than, the differences in the inner turning points. In any case, any differences in the locations of the centres of sensitivities are minute compared to both the spread implied by the posterior distribution on Δt, and the localisation widths of the pooled kernels themselves (indicated with the horizontal intervals). Thus, without access to the individual rotational splittings, our constrained modification to the OLA techique is unfortunately unable to pin down the location, or even direction, of the implied rotational shear in the envelope.

The preceding discussion has implicitly relied on a two-zone model of radial differential rotation, where we have used the separation between pooled dipole and quadrupole modes to provide us both the averaged rotation rate in these two zones, as well as the locations of the zones themselves. Since the underlying rotational kernels have proven uncooperative in allowing us to distinguish the locations of these two zones, we may instead make this assumption explicit by parameterising $\Omega(t)$ to contain two physically separated regions of solid-body rotation, with a shear layer between the two. More concretely, we describe the rotational profile as

$$\Omega(t;\Omega_{\mathrm{in}},\Omega_{\mathrm{out}},t_{\mathrm{shear}},\Delta t) = \Omega_{\mathrm{in}} + \left(\frac{\Omega_{\mathrm{out}}-\Omega_{\mathrm{in}}}{2}\right)\left(\tanh\left(\frac{t-t_{\mathrm{shear}}}{\Delta t}\right)+1\right), \tag{B3}$$

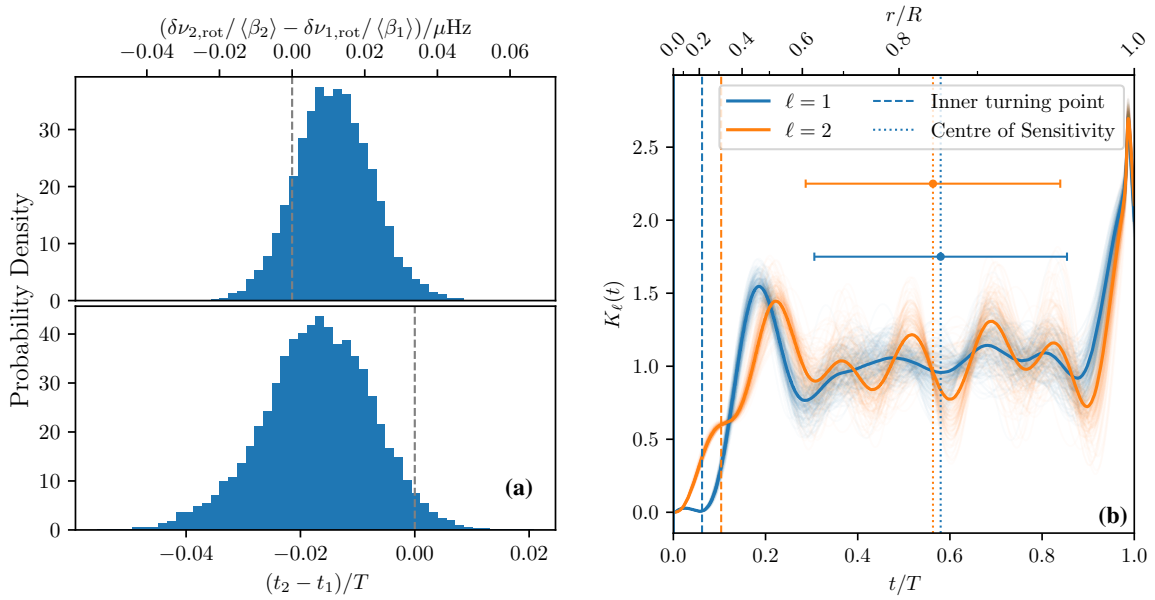

Figure B2. Raw asteroseismic constraints on sensitivity to rotational shear. **(a)** Posterior distributions for differences between the pooled quadrupole and dipole rotational splitting. The upper panel shows the posterior distribution of the differences in estimated rotation rates, which are in turn the rotational splittings divided by effective sensitivity constants $\langle\beta_\ell\rangle \sim 1$. The lower panel shows the posterior distribution of the differences in acoustic radii of the centres of sensitivity associated with the underlying averaged rotational kernels of each degree, considered separately. The two quantities are statistically independent. **(b)** Differential sensitivity kernels associated with distributions in (a). Associated with each pooled rotational splitting $\delta\nu_\ell$ is an effective rotational kernel K_ℓ, which is a weighted average of the rotational kernels associated with each mode of that degree. Faint curves show samples from the posterior distribution, while the solid coloured curves show the posterior median effective kernel for each degree. The inner turning points at ν_{max} of the best fitting stellar model from our optimisation procedure are shown with the vertical dashed lines, while the centres of sensitivity for the median kernels are indicated with the vertical dotted lines. The ordering of their positions can be seen to reversed compared to the theoretical inner turning points. The localisation widths of the median kernels are indicated by the horizontal intervals placed around the centres of sensitivity.

which we use to generate predictions for the rotational splittings through Eq. (B1), as done in the RLS technique. Rather than comparing these predictions against measured rotational splittings (which we do not have in hand), we may instead constrain the parameters $(\Omega_{\mathrm{in}}, \Omega_{\mathrm{out}}, t_{\mathrm{shear}}, \Delta t)$ of this description directly against the power spectrum, by inserting these predictions into our parametric model of the power spectrum, Eq. (2), in lieu of the pooled rotational splittings, and evaluating likelihoods using the same χ^2-2-degree-of-freedom likelihood function (Eq. (3)) as we had earlier used for the pooled rotational splittings. This allows us to derive posterior distributions for these parameters of Eq. (B3) (and the other existing parameters of the model) through the same nested sampling procedure as we had used in Section 2.1. For this purpose, we place the same uniform priors on $\Omega_{\mathrm{bulk}} = (\Omega_{\mathrm{in}} + \Omega_{\mathrm{out}})/2$ as we did on the pooled rotational splittings in Section 2.1 (up to factor of 2π), and we also place very wide uniform priors on $\Delta\Omega = \Omega_{\mathrm{out}} - \Omega_{\mathrm{in}}$, permitting it to vary between -0.016 μHz and $+0.016$ μHz — i.e. our prior is chosen explicitly so as not to favour either sense of the rotational shear.

We show the resulting joint posterior distribution for these parameters, together with the inclination, using blue points, contours, and histograms, in Fig. B3a. As we encountered in our earlier discussion of the rotational kernels, even this regularised construction is unable to constrain the location, or the sharpness, of the rotational shear. However, as above, it appears to also weakly favour a sense of the rotational shear where the interior of the convective envelope is rotating faster than the exterior. To better illustrate this, we show in Fig. B3b several random samples for the posterior distribution over possible shapes of $\Omega(r)$, using the thin faint curves. These curves are coloured blue if $\Omega_{\mathrm{in}} > \Omega_{\mathrm{out}}$, and red otherwise. The overall median rotational profile, which we show with the solid black curve, is such that the rotation rate decreases outwards. Nonetheless, we cannot rule out the opposite sense of differential rotation, as some rotational profiles in the converse sense (i.e. increasing outwards, shown in red) are encompassed within the 1σ-credible region, shown with the dashed black curves.

Differential rotation in the sense of Ω decreasing outwards would possibly require a second shear layer to exist near the the surface, not described by Eq. (B3), for consistency with the photometric rotation rate. This shear layer would also have to be located very near the surface, in order not to overly affect values returned from the integral expression in Eq. (B1) from the low-degree kernels that we have access to.

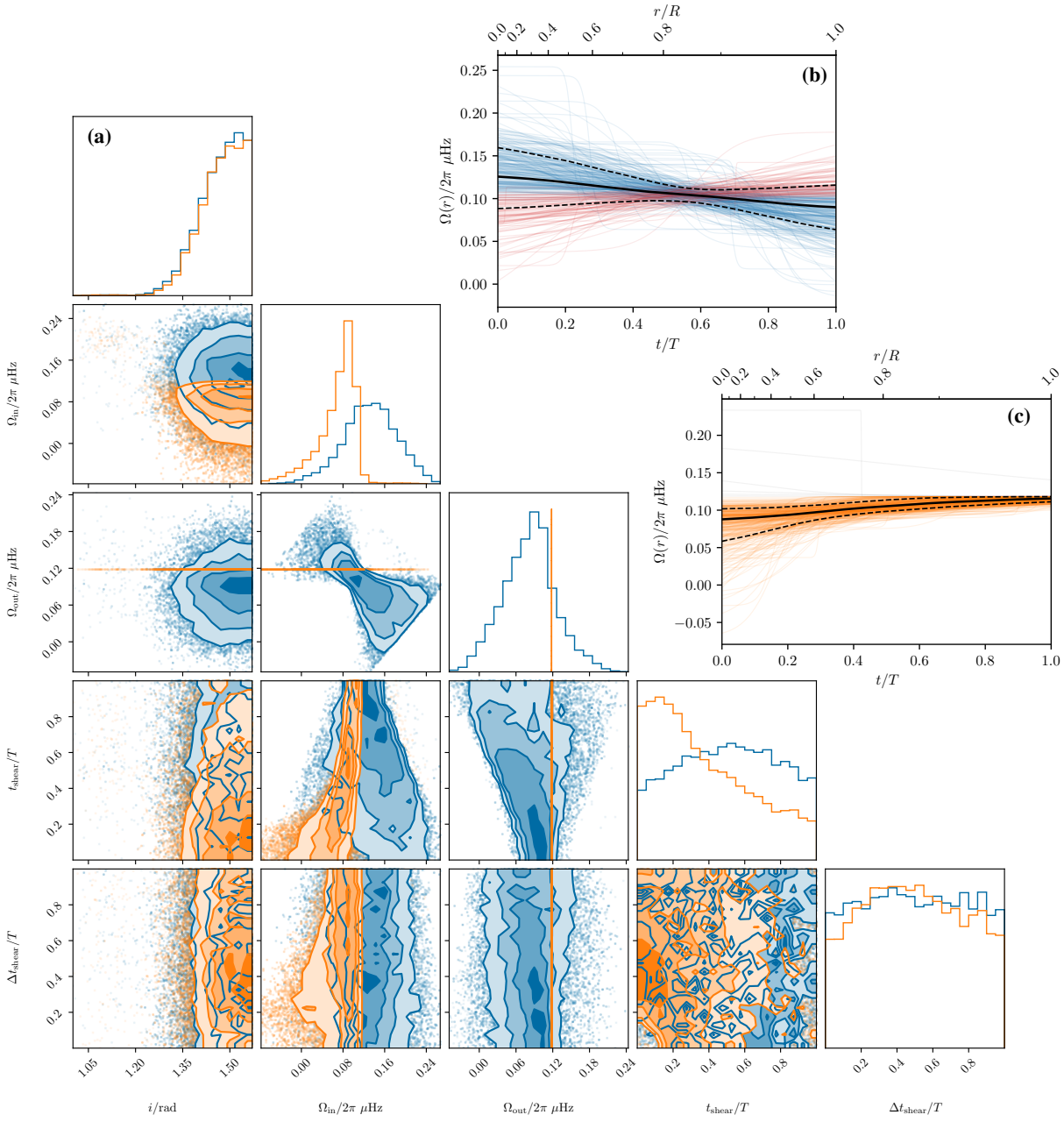

Figure B3. Regularised asteroseismic constraints on rotational shear. **(a)** Joint posterior distributions for the stellar inclination, inner and outer rotation rates, location, and thickness of the rotational shear layer, which parameterise our regularised two-zone description of the rotational profile, Eq. (B3). We show in blue the posterior distributions obtained from the power spectrum with the flat priors described in the main text, and with orange a conditional distribution obtained by demanding that the outer rotation rate matches the value provided by photometry. **(b)** Samples from the posterior distribution over rotational profiles from the main exercise are shown with the thin faint lines. These are coloured blue if they are consistent with differential rotation in the sense of the rotation rate decreasing towards the surface, and red for the converse sense. The median rotational profile is shown with the thick black curve, and the $\pm 1\sigma$ posterior credible region around it is demarcated with the dashed curves. **(c)** The same as (b), but for our restricted scenario where the outer rotation rate is matched to the photometric value. Draws from the posterior distribution with the rotation rate increasing outwards are shown in orange, while those with the converse sense of differential rotation are shown in gray.

Such an asteroseismically inaccessible (at least at low degree) near-surface shear layer is not strictly speaking impossible. Indeed, it is the preferred explanation adopted by Tayar et al. (2022) to explain the rotational configuration of the red giant considered in that work, whose surface rotation rate, obtained from spectroscopy, is similarly faster than a pooled estimate of bulk rotation in the envelope recovered from the quadrupole and octupole p-modes. A near-surface shear layer (albeit with rotational shear in the opposite sense, and at different optical depth than demanded here) is also known to exist in the Sun, where its presence is confirmed by the observational availability of intermediate and high-degree modes, whose rotational kernels, being confined almost entirely to the near-surface layers, would not find it similarly invisible (e.g. Schou et al. 1998; Howe 2009).

However, without measurements of modes of intermediate or high degree available, we cannot claim that this explanation is unique. For one, although we have so far discussed differential rotation in only the radial direction, it is possible that it also exists latitudinally. While the spherical harmonics of the sectoral modes through which we observe the rotational splitting are sensitive mostly to an equatorial band (i.e. $P_\ell^\ell(\cos\theta)$ can be expressed in terms of only $\sin\theta$: Arfken & Weber 2005), the latitudes of the surface features producing our photometric rotational signal are entirely unconstrained. Should they be located at high latitude, and should Zvrk additionally exhibit latitudinal differential rotation in an anti-solar sense, then we would expect its equator to be rotating more slowly than the photometric modulations would imply; this would resolve our discrepancy from purely geometrical considerations. However, such an explanation would be fairly ad-hoc, as it would require Zvrk's surface features to persist at much higher latitudes than the spots on magnetically active stars. In any case, latitudinal differential rotation in general, and on stars that are not Sun-like in particular, is very poorly understood.

We can also explore alternative solutions to this issue by further regularising our asteroseismic inferences. To demonstrate this, we repeat our nested-sampling exercise, but further demand that $\Omega_{\rm out}$ match our photometric surface rotational period of 99 days (i.e. we place a δ-function prior on $\Omega_{\rm out}$). We place a uniform prior on $\Omega_{\rm in}$ centered on this value, extending 0.016 μHz in both directions — again, so as not to favour either sense of the rotational shear a priori. In this fashion, we recover a conditional posterior distribution for the scenario where the outer rotation rate of the convective envelope matches the surface. We show the results of this procedure in Fig. B3a using the orange points, contours, and histograms.

Under this more restrictive scenario, the inferred conditional posterior distribution on $\Omega_{\rm in}$ can now be seen to favour differential rotation in the sense of Ω increasing outwards. This can also be seen when we examine the implied conditional distribution over the rotational profiles themselves, shown in Fig. B3c, where sampled profiles which increase outwards are shown in orange, and those which do not are shown in gray: the latter can be seen to be exceedingly rare. However, we see also that the imposition of this hard prior on $\Omega_{\rm out}$ also requires $t_{\rm shear}$ to be situated much farther away from the surface, as can be seen from the strong peak in its marginal distribution in Fig. B3a, at roughly $t/T \sim 0.1$ (i.e. $r/R \sim 0.3$ in our best-fitting stellar structure), as opposed to naturally producing a near-surface shear layer as we originally posited. This does not, however, contraindicate the existence of such a near-surface shear layer, as we have little a priori justification for adopting such a δ-function prior on $\Omega_{\rm out}$ in the first place.

REFERENCES

Abdurro'uf, Accetta, K., Aerts, C., et al. 2022, ApJS, 259, 35
Aerts, C., Mathis, S., & Rogers, T. M. 2019, ARA&A, 57, 35
Aguilera-Gómez, C., Chanamé, J., Pinsonneault, M. H., & Carlberg, J. K. 2016a, ApJ, 829, 127
—. 2016b, ApJL, 833, L24
Ahlborn, F., Bellinger, E. P., Hekker, S., Basu, S., & Mokrytska, D. 2022, A&A, 668, A98
Anderson, E. R., Duvall, Thomas L., J., & Jefferies, S. M. 1990, ApJ, 364, 699
Arfken, G. B., & Weber, H. J. 2005, Mathematical methods for physicists 6th ed.
Asplund, M., Grevesse, N., Sauval, A. J., & Scott, P. 2009, ARA&A, 47, 481
Astropy Collaboration, Robitaille, T. P., Tollerud, E. J., et al. 2013, A&A, 558, A33
Astropy Collaboration, Price-Whelan, A. M., Sipőcz, B. M., et al. 2018, AJ, 156, 123
Avallone, E. A., Tayar, J. N., van Saders, J. L., et al. 2022, ApJ, 930, 7
Backus, G., & Gilbert, F. 1968, Geophysical Journal, 16, 169
Ball, W. H., & Gizon, L. 2014, A&A, 568, A123
Ball, W. H., Themeßl, N., & Hekker, S. 2018, MNRAS, 478, 4697
Bouvier, J., Lanzafame, A. C., Venuti, L., et al. 2016, A&A, 590, A78
Bromley, B. C., Leonard, A., Quintanilla, A., et al. 2021, AJ, 162, 98
Brun, A. S., & Browning, M. K. 2017, Living Reviews in Solar Physics, 14, 4
Cameron, A. G. W., & Fowler, W. A. 1971, ApJ, 164, 111
Campante, T. L., Li, T., Ong, J. M. J., et al. 2023, AJ, 165, 214
Cao, L., & Pinsonneault, M. H. 2022, MNRAS, 517, 2165
Carlberg, J. K., Majewski, S. R., Patterson, R. J., et al. 2011, ApJ, 732, 39
Casey, A. R., Ho, A. Y. Q., Ness, M., et al. 2019, ApJ, 880, 125
Ceillier, T., Tayar, J., Mathur, S., et al. 2017, A&A, 605, A111
Chatterjee, S., Ford, E. B., Matsumura, S., & Rasio, F. A. 2008, ApJ, 686, 580
Christensen-Dalsgaard, J. 2008, Ap&SS, 316, 113
Christensen-Dalsgaard, J., Schou, J., & Thompson, M. J. 1990, MNRAS, 242, 353
Christensen-Dalsgaard, J., Silva Aguirre, V., Cassisi, S., et al. 2020, A&A, 635, A165
Claytor, Z. R., van Saders, J. L., Llama, J., et al. 2022, ApJ, 927, 219
Cunha, M. S., Roxburgh, I. W., Aguirre Børsen-Koch, V., et al. 2021, MNRAS, 508, 5864
De, K., MacLeod, M., Karambelkar, V., et al. 2023, Nature, 617, 55
Deheuvels, S., Ballot, J., Eggenberger, P., et al. 2020, A&A, 641, A117
Deheuvels, S., Ballot, J., Gehan, C., & Mosser, B. 2022, A&A, 659, A106
Deheuvels, S., Ouazzani, R. M., & Basu, S. 2017, A&A, 605, A75
Deming, D., Knutson, H., Kammer, J., et al. 2015, ApJ, 805, 132
Eggenberger, P., Buldgen, G., & Salmon, S. J. A. J. 2019a, A&A, 626, L1
Eggenberger, P., den Hartogh, J. W., Buldgen, G., et al. 2019b, A&A, 631, L6
Eggleton, P. P. 1983, ApJ, 268, 368
Eggleton, P. P., & Kiseleva-Eggleton, L. 2001, ApJ, 562, 1012

Farnir, M., Pinçon, C., Dupret, M. A., Noels, A., & Scuflaire, R. 2021, A&A, 653, A126
Fellay, L., Buldgen, G., Eggenberger, P., et al. 2021, A&A, 654, A133
Fuller, J., Piro, A. L., & Jermyn, A. S. 2019, MNRAS, 485, 3661
Gaia Collaboration, Brown, A. G. A., Vallenari, A., et al. 2018, A&A, 616, A1
Gaulme, P., Jackiewicz, J., Spada, F., et al. 2020, A&A, 639, A63
Gehan, C., Gaulme, P., & Yu, J. 2022, A&A, 668, A116
Gehan, C., Mosser, B., Michel, E., & Cunha, M. S. 2021, A&A, 645, A124
Gehan, C., Mosser, B., Michel, E., Samadi, R., & Kallinger, T. 2018, A&A, 616, A24
Gizon, L., & Solanki, S. K. 2003, ApJ, 589, 1009
Gough, D. 1985, SoPh, 100, 65
Gough, D. O. 1981, MNRAS, 196, 731
Gough, D. O., & Thompson, M. J. 1990, MNRAS, 242, 25
Goupil, M. J., Mosser, B., Marques, J. P., et al. 2013, A&A, 549, A75
Grevesse, N., & Sauval, A. J. 1998, SSRv, 85, 161
Harris, C. R., Millman, K. J., van der Walt, S. J., et al. 2020, Nature, 585, 357
Hart, K., Shappee, B. J., Hey, D., et al. 2023, arXiv e-prints, arXiv:2304.03791
Hayes, C. R., Masseron, T., Sobeck, J., et al. 2022, ApJS, 262, 34
Howe, R. 2009, LRSP, 6, 1
Hut, P. 1981, A&A, 99, 126
Ivezić, Ž., Connolly, A. J., VanderPlas, J. T., & Gray, A. 2014, Statistics, Data Mining, and Machine Learning in Astronomy: A Practical Python Guide for the Analysis of Survey Data, doi: 10.1515/9781400848911
Jia, S., & Spruit, H. C. 2018, ApJ, 864, 169
Jiang, C., Cunha, M., Christensen-Dalsgaard, J., Zhang, Q. S., & Gizon, L. 2022, MNRAS, 515, 3853
Kamiaka, S., Benomar, O., & Suto, Y. 2018, MNRAS, 479, 391
Kennedy, G. M., & Kenyon, S. J. 2008, ApJ, 673, 502
Klion, H., & Quataert, E. 2017, MNRAS, 464, L16
Knutson, H. A., Fulton, B. J., Montet, B. T., et al. 2014, ApJ, 785, 126
Kochanek, C. S., Shappee, B. J., Stanek, K. Z., et al. 2017, PASP, 129, 104502
Koposov, S., Speagle, J., Barbary, K., et al. 2022, joshspeagle/dynesty: v2.0.1, v2.0.1, Zenodo, Zenodo, doi: 10.5281/zenodo.7215695
Kraus, A. L., & Rizzuto, A. 2022, adamkraus/comove. https://github.com/adamkraus/Comove
Lau, M. Y. M., Cantiello, M., Jermyn, A. S., et al. 2022, arXiv e-prints, arXiv:2210.15848
Lindsay, C. J., Ong, J. M. J., & Basu, S. 2023, accepted to ApJ, arXiv:2304.06770
Lomb, N. R. 1976, Ap&SS, 39, 447
Lu, Y., Angus, R., Agüeros, M. A., et al. 2020, AJ, 160, 168
Martell, S. L., Simpson, J. D., Balasubramaniam, A. G., et al. 2021, MNRAS, 505, 5340
Massarotti, A., Latham, D. W., Stefanik, R. P., & Fogel, J. 2008, AJ, 135, 209
Mier, P. R. 2017, Pablormier/Yabox: V1.0.3, v1.0.3, Zenodo, doi: 10.5281/zenodo.848679
Million, C., Fleming, S. W., Shiao, B., et al. 2016, ApJ, 833, 292
Mosser, B., Gehan, C., Belkacem, K., et al. 2018, A&A, 618, A109
Mosser, B., Belkacem, K., Goupil, M. J., et al. 2011, A&A, 525, L9
Mosser, B., Goupil, M. J., Belkacem, K., et al. 2012, A&A, 548, A10
Mosser, B., Benomar, O., Belkacem, K., et al. 2014, A&A, 572, L5
Naoz, S., Farr, W. M., Lithwick, Y., Rasio, F. A., & Teyssandier, J. 2011, Nature, 473, 187
—. 2013, MNRAS, 431, 2155
Naoz, S., Farr, W. M., & Rasio, F. A. 2012, ApJL, 754, L36
Nielsen, M. B., Davies, G. R., Ball, W. H., et al. 2021, AJ, 161, 62
Nikutta, R., Hunt-Walker, N., Nenkova, M., Ivezić, Ž., & Elitzur, M. 2014, MNRAS, 442, 3361
Noyes, R. W., Hartmann, L. W., Baliunas, S. L., Duncan, D. K., & Vaughan, A. H. 1984, ApJ, 279, 763
O'Connor, C. E., Bildsten, L., Cantiello, M., & Lai, D. 2023, arXiv e-prints, arXiv:2304.09882
Ong, J. M. J., & Basu, S. 2019, ApJ, 885, 26
—. 2020, ApJ, 898, 127
Ong, J. M. J., Basu, S., & McKeever, J. M. 2021, ApJ, 906, 54
Ong, J. M. J., Bugnet, L., & Basu, S. 2022, ApJ, 940, 18
Ong, J. M. J., & Gehan, C. 2023, ApJ, 946, 92
Paladini, C., Baron, F., Jorissen, A., et al. 2018, Nature, 553, 310
Patton, R. A., Pinsonneault, M. H., Cao, L., et al. 2023, submitted to MNRAS, arXiv:2303.08151
Paxton, B., Bildsten, L., Dotter, A., et al. 2011, ApJS, 192, 3
Paxton, B., Cantiello, M., Arras, P., et al. 2013, ApJS, 208, 4
Paxton, B., Marchant, P., Schwab, J., et al. 2015, ApJS, 220, 15
Paxton, B., Schwab, J., Bauer, E. B., et al. 2018, ApJS, 234, 34
Paxton, B., Smolec, R., Schwab, J., et al. 2019, ApJS, 243, 10
Pesnell, W. D. 1985, ApJ, 292, 238
Pijpers, F. P., & Thompson, M. J. 1994, A&A, 281, 231
Pinsonneault, M. H., Elsworth, Y. P., Tayar, J., et al. 2018, ApJS, 239, 32
Pinsonneault, M. H., et al. in prep.
Qureshi, A., Naoz, S., & Shkolnik, E. L. 2018, ApJ, 864, 65
Reback, J., Mendel, J. B., McKinney, W., et al. 2021, pandas-dev/pandas: Pandas 1.3.0, v1.3.0, Zenodo, doi: 10.5281/zenodo.3509134
Reimers, D. 1975, Memoires of the Societe Royale des Sciences de Liege, 8, 369
Rizzuto, A. C., Ireland, M. J., & Robertson, J. G. 2011, MNRAS, 416, 3108
Rizzuto, A. C., Vanderburg, A., Mann, A. W., et al. 2018, AJ, 156, 195
Roxburgh, I. W. 2010, Ap&SS, 328, 3
—. 2016, A&A, 585, A63
Scargle, J. D. 1982, ApJ, 263, 835
Schou, J., Antia, H. M., Basu, S., et al. 1998, ApJ, 505, 390
Schunker, H., Schou, J., & Ball, W. H. 2016a, A&A, 586, A24
Schunker, H., Schou, J., Ball, W. H., Nielsen, M. B., & Gizon, L. 2016b, A&A, 586, A79
Serenelli, A., Johnson, J., Huber, D., et al. 2017, ApJS, 233, 23
Shappee, B. J., Prieto, J. L., Grupe, D., et al. 2014, ApJ, 788, 48
Sharma, S., Stello, D., Bland-Hawthorn, J., Huber, D., & Bedding, T. R. 2016, ApJ, 822, 15
Soares-Furtado, M., Cantiello, M., MacLeod, M., & Ness, M. K. 2021, AJ, 162, 273
Stello, D., Compton, D. L., Bedding, T. R., et al. 2014, ApJL, 788, L10
Stephan, A. P., Naoz, S., & Gaudi, B. S. 2018, AJ, 156, 128
—. 2021, ApJ, 922, 4
Stephan, A. P., Naoz, S., Gaudi, B. S., & Salas, J. M. 2020, ApJ, 889, 45
Tayar, J., & Joyce, M. 2022, ApJL, 935, L30
Tayar, J., Ceillier, T., García-Hernández, D. A., et al. 2015, ApJ, 807, 82
Tayar, J., Moyano, F. D., Soares-Furtado, M., et al. 2022, ApJ, 940, 23
Thompson, T. A., Kochanek, C. S., Stanek, K. Z., et al. 2019, Science, 366, 637
Townsend, R. H. D., & Teitler, S. A. 2013, MNRAS, 435, 3406
Triana, S. A., Corsaro, E., De Ridder, J., et al. 2017, A&A, 602, A62
van Saders, J. L., & Pinsonneault, M. H. 2013, ApJ, 776, 67
VanderPlas, J. T. 2018, ApJS, 236, 16
Vaňko, M., Torres, G., Hambálek, L., et al. 2017, MNRAS, 467, 4902
Viani, L. S., Basu, S., Corsaro, E., Ball, W. H., & Chaplin, W. J. 2019, ApJ, 879, 33
Viani, L. S., Basu, S., Ong, J. M. J., Bonaca, A., & Chaplin, W. J. 2018, ApJ, 858, 28
Virtanen, P., Gommers, R., Oliphant, T. E., et al. 2020, NatMe, 17, 261
Wang, E. X., Nordlander, T., Asplund, M., et al. 2021, MNRAS, 500, 2159
Weidenschilling, S. J., & Marzari, F. 1996, Nature, 384, 619
White, T. R., Bedding, T. R., Stello, D., et al. 2011, ApJ, 743, 161
Wittenmyer, R. A., Wang, S., Horner, J., et al. 2020, MNRAS, 492, 377
Wright, E. L., Eisenhardt, P. R. M., Mainzer, A. K., et al. 2010, AJ, 140, 1868
Xing, L. F. 2010, ApJ, 723, 1542
Yarza, R., Razo Lopez, N., Murguia-Berthier, A., et al. 2023, accepted to ApJ, arXiv:2203.11227
Yu, J., Bedding, T. R., Stello, D., et al. 2020, MNRAS, 493, 1388